The solid-state DNP effect in liquids

Deniz Sezer

Institute of Physical and Theoretical Chemistry, Goethe University, 60438 Frankfurt am Main, Germany

Correspondence: Deniz Sezer (dzsezer@gmail.com)

Abstract. The solid-state effect of dynamic nuclear polarization (DNP) is operative also in viscous liquids where the dipolar interaction between the electronic and nuclear spins is partially averaged. The proper way to quantify the degree of averaging, and thus calculate the efficiency of the effect, should be based on the time-correlation function of the dipolar interaction. Here we use the stochastic Liouville equation formalism to develop a general theoretical description of the solid effect in liquids. The derived expressions can be used with different dipolar correlations functions depending on the assumed motional model. At high magnetic fields, the theory predicts DNP enhancements at small offsets, far from the classical solid-effect positions that are displaced by one nuclear Larmor frequency from the electronic resonance. The predictions are in quantitative agreement with such enhancement peaks observed at 9.4 T [Kuzhelev et al. *JACS* **144**, 1164 (2022)]. These non-canonical peaks are not due to thermal mixing or the cross effect but exactly follow the dispersive component of the EPR line.

1 Introduction

The last two decades have witnessed an overarching development in nuclear hyperpolarization techniques across the entire spectrum of mechanisms, from the classical Overhauser and solid-state effects to (photo)chemically-induced and parahydrogen-based polarization (Eills et al., 2023). While the majority of the reported applications have relied on polarization transfer in the solid state at cryogenic temperatures (Ni et al., 2013; Pinon et al., 2021), transfer in the liquid state at elevated (room or physiological) temperatures has also been actively explored (Prisner et al., 2016; Denysenkov et al., 2022). In the liquid state, the mechanism of polarization has almost exclusively been the Overhauser effect (Jakdetchai et al., 2014). One notable exception is the work of Stapf and coworkers in which the solid effect of dynamic nuclear polarization (DNP) has been employed in combination with field-cycling relaxometry to characterize the molecular dynamics in ionic liquids and polymer melts at ambient temperatures (Neudert et al., 2017; Gizatullin et al., 2019, 2021b, a, 2022).

At X band (9.6 GHz/0.35 T), where the DNP measurements of Stapf and colleagues have been carried out, the nuclear Larmor frequencies of ^{1}H and ^{19}F ($\omega_I \approx 15$ MHz) are less than the EPR spectral width of a nitroxide free radical, and even comparable to the spectral width of the single-line radical BDPA (Gizatullin et al., 2021b). As a result, the negative and positive solid-effect enhancements overlap and partly cancel each other, complicating the quantitative analysis of the effect. An additional difficulty for quantification is that, in many instances, the Overhauser and solid effects coexist (Leblond et al., 1971b; Neudert et al., 2017; Gizatullin et al., 2022). Although the contributions of these two effects can generally be distinguished on the basis of

their even (Overhauser effect) and odd (solid effect) parity with the offset from the electronic resonance, this identification could be complicated when the EPR spectrum is broad and asymmetrical.

To quantify the field profile of the DNP enhancement (i.e., the DNP spectrum), Stapf and colleagues use a weighted sum of (i) the EPR line shape (for the Overhauser effect) and (ii) the same line shape shifted by $\pm\omega_I$, with one of the shifted copies flipped around the vertical axis (for the solid effect) (Neudert et al., 2017; Gizatullin et al., 2021b). The relative contribution of the two effects is then treated as a fitting parameter. In general, the resulting fits are in good overall agreement with the experimental DNP spectra, but oftentimes there are quantitative deviations. Recently, the remaining discrepancy between the experimental and calculated DNP spectra was interpreted as evidence for the simultaneous occurrence of a third DNP mechanism, in addition to the Overhauser and solid effects (Gizatullin et al., 2022).

In the companion paper (Paper I) we showed that when the mw nutation frequency approaches the nuclear Larmor frequency, as could be the case at X band under the high mw powers used in the DNP experiments (Neudert et al., 2016), the forbidden transitions of the solid effect are no longer shifted by $\pm\omega_I$ with respect to the electronic resonance but come closer together, and may even coalesce (Sezer, 2023). In such cases, the theoretical justification for modeling the solid effect field profile by shifting the EPR line shape by $\pm\omega_I$ becomes questionable. Unfortunately, the analytical expressions of Paper I, which remain valid in this regime, are not applicable to liquids since they do not account for the modulation of the dipolar interaction by molecular diffusion. In the current paper, the time-domain description of the solid effect from Paper I is extended to liquids.

Recently, Kuzhelev et al. (2022) reported proton DNP enhancements in the liquid phase of lipid bilayers at 9.4 T (260 GHz) using the free radical BDPA as a polarizing agent. The large nuclear Larmor frequency (400 MHz) enabled a clear spectral separation of the acyl-chain protons and the polar protons of water. For the non-polar protons, maximal enhancements were observed at the canonical resonance positions of the zero- and double-quantum forbidden transitions, characteristic of the solid effect, while enhancement due to the Overhauser effect was missing. The large spectral separation of the positive and negative enhancements, and the narrow line of BDPA provided a uniquely "clean" access to the solid effect in a viscous liquid environment (Kuzhelev et al., 2022).

In addition to the maximum enhancements at the canonical solid effect offsets, the DNP spectrum of Kuzhelev et al. (2022) revealed additional enhancement peaks at much smaller offsets. These were postulated to arise due to the DNP mechanism known as thermal mixing. However, thermal mixing is commonly associated with a broad EPR spectrum (Wenckebach, 2021), while the spectrum of BDPA was extremely narrow at the elevated DNP concentration used in the experiment, and the observed spurious enhancement peaks lay outside this narrow spectrum (Kuzhelev et al., 2022, fig. 2). Here we explain the entire DNP spectrum, including the puzzling features at low offsets, considering only one electronic and one nuclear spin.

The rest of the paper is organized as follows. To account for molecular diffusion, in Sec. 3 we transform the equations of motion of Paper I into stochastic Liouville equations (SLEs) (Kubo, 1969). After taking into account that all relevant time scales are orders of magnitude shorter than the nuclear spin-lattice relaxation time, the SLE formalism yields the time-correlation function of the dipolar interaction. In Sec. 4 we show that the solid-effect lines in the DNP spectrum (i.e., those shifted by $\pm\omega_I$) experience additional motional broadening compared to the homogeneous EPR line width. As a result, the tails of these lines around the position of the electronic resonance increase substantially. Under favorable conditions, the product of

these tails with the dispersive EPR component may become sufficiently large to be visible as separate enhancement peaks in the DNP field profile. We attribute the non-canonical peaks in the DNP spectrum of Kuzhelev et al. (2022) to this phenomenon. Our conclusions are presented in Sec. 5. The next section summarizes the needed background.

2   Motivation and background

2.1   Dynamic nuclear polarization in liquids

The transfer of polarization in solids involves two mechanistically different steps (Hovav et al., 2010; Smith et al., 2012). The first one is the direct polarization of the nuclear spins that are sufficiently close to the free radical and have appreciable dipole-dipole interaction with the electronic spin. Being closest to the unpaired electron, the nuclei on the free radical itself benefit most from this first step of direct polarization (Tan et al., 2019; Delage-Laurin et al., 2021). Polarizing the intramolecular nuclei in this way, however, is not particularly useful unless the polarization can spread to the rest of the sample. This is where the second step comes in. In this step, the polarization spreads from the directly polarized nuclei to the distant nuclei by spin diffusion. Because it relies on the relatively weak dipole-dipole interaction between the nuclear spins, spin diffusion is slow and is often the bottleneck for efficient polarization transfer in the solid state (Hovav et al., 2010; Wiśniewski et al., 2016).

In liquids, spin diffusion is not efficient because the nuclei constantly change their positions due to random thermal motions. However, since molecular diffusion moves the nuclei across nanometer distances in nanoseconds, and thus rapidly spreads the polarization of the directly polarized nuclei across the sample, spin diffusion is also not needed. Taking glycerol as an example, with a self-diffusion coefficient of 6.6×10^{-3} nm^2/ns at 40°C (Tomlinson, 1973), which is 500 times less than the self-diffusion coefficient of water at the same temperature (Holz et al., 2000), it is a rather viscous liquid. Nevertheless, at the relatively small radical concentration of 1 mM, a molecule of glycerol covers the average distance between two radicals in less than 400 ns. This is at least five orders of magnitude less than the nuclear T_1 of protons, even after accounting for paramagnetic relaxation. Any given solvent nucleus will thus encounter the electronic spins a million times during its T_1 relaxation time. Even in viscous liquids, therefore, molecular diffusion is expected to homogenize the nuclear polarization across the sample during times that are orders of magnitude shorter than the nuclear T_1. This advantage of liquids over solids, however, comes at a price: the polarization of the nuclei on the free radical is no longer accessible to the solvent, and proximal solvent nuclei have to be polarized directly in the first step of polarization transfer (fig. 1).

Given that every solvent molecule gets directly polarized and also spreads the polarization, the distinction between the two steps of polarization transfer in liquids (fig. 1) is conceptual and does not reflect fundamental differences in the mechanisms of the two steps. In fact, both steps are enabled by molecular diffusion which sometimes brings a solvent molecule closer to the radical and sometimes takes it further away. Since the analytical description of translational diffusion in simple liquids is well developed (Ayant et al., 1975; Hwang and Freed, 1975), a unified theoretical treatment of the two steps of polarization transfer becomes possible, as we demonstrate in the present paper.
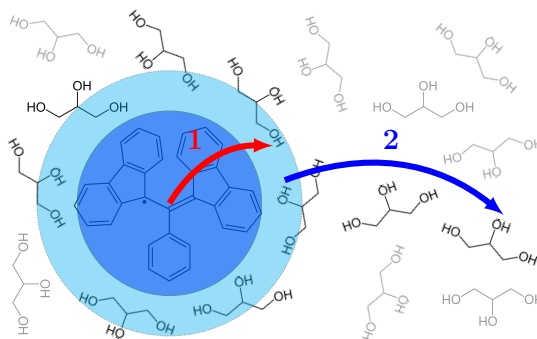
Figure 1. Two conceptually different steps of the polarization transfer process in liquids. 1. Direct transfer from the electronic spin on the free radical to the proximate nuclear spins on the solvent molecules due to dipolar interaction. 2. Diffusion of the proximate solvent molecules to the bulk.

From the six terms of the dipolar alphabet, the part that contributes to the solid effect is $A_1 S_z I_+ + A_1^* S_z I_-$ (Wenckebach, 2016) where

$$A_1 = D_{\text{dip}} \frac{-3 \cos\theta \sin\theta \, \mathrm{e}^{-\mathrm{i}\phi}}{r^3}. \tag{1}$$

95 Here $D_{\text{dip}} = (\mu_0/4\pi)\hbar\gamma_S\gamma_I$ is the dipolar constant and (r, θ, ϕ) are the spherical polar coordinates of the vector pointing from the electronic spin to the nuclear spin. (γ_S and γ_I are the gyromagnetic ratios of the electronic and nuclear spins.) The angular dependence of A_1 is that of a second-degree spherical harmonic of order $m = 1$, as implied by the subscript. The need for direct polarization of the solvent nuclei in liquids increases the shortest possible distance r in (1) and thus reduces the largest achievable dipolar coupling. This requirement for interaction across a larger distance, however, does not explain why the solid

100 effect works in solids but is compromised in liquids.

To understand the difference between solids and liquids one should consider the time-correlation function of the dipolar interaction:

$$C_{11}(t) = \langle\langle A_1^*(t' + t) A_1(t') \rangle_{t'}\rangle. \tag{2}$$

Here the inner angular brackets with the subscript t' denote averaging with respect to the time point t' along the random

105 trajectory of a single nuclear spin. Because every nucleus encounters the electronic spins millions of times during its T_1 relaxation time, this average should be the same for all nuclei in the liquid. Thus, in addition to the time averaging, in (2) we also average over the ensemble of identical nuclear spins in the sample (outer angular brackets).

Now, if the dipolar correlation function (2) decays on time scales that are much longer than some relevant characteristic time, then the experiment essentially detects the initial value $C_{11}(0) = \langle\langle A_1^*(t') A_1(t') \rangle_{t'}\rangle = \langle A_1^* A_1 \rangle$. The last ensemble average over

110 all electron-nucleus pairs requires integration over the spatial variables (r, θ, ϕ) and multiplication by the concentration N of

the unpaired electrons:

$$\langle A_1^* A_1 \rangle = N D_{\text{dip}}^2 \frac{24\pi}{5} \int\limits_b^\infty \frac{\mathrm{d}r}{r^4} = D_{\text{dip}}^2 \frac{24\pi}{5} \frac{N}{3b^3}. \tag{3}$$

(The factor $24\pi/5$ comes from the normalization of the spherical harmonic Y_2^1.) This slow-motional limit corresponds to the situation in solids under the (unrealistic) assumption of fast and efficient spin diffusion. If, on the other hand, the decay time of the correlation function is much shorter than the relevant characteristic time scale, then the experiment detects the long-time limit $C_{11}(\infty) = \langle\langle A_1^*(\infty) A_1(t')\rangle_{t'}\rangle = \langle A_1^*\rangle\langle A_1\rangle$. The solid effect vanishes because the average of the spherical harmonic Y_2^1 over the angles gives $\langle A_1 \rangle = 0$. This fast-motional limit corresponds to low-viscosity liquids in which the dipolar interaction is averaged out. To the extent that they exhibit the solid effect, viscous liquids must lie somewhere between these two extremes.

The interpolation between these two limiting cases on the basis of the dipolar correlation function is formally developed in Sec. 3. This task requires a time-domain description of the solid effect, similar to the treatment of relaxation by random motion where the correlation function arises from second-order, time-dependent perturbation theory. In principle, there are two such time-domain descriptions that we can utilize for the treatment of the solid effect in liquids. The first is the rate-equation formalism, which models the dynamics of the electronic and nuclear polarizations, and the second is the description that we developed in Paper I, which additionally accounts for the dynamics of the coherences. Both of these options will be explored in Sec. 3. When modeling the stochastic dynamics of the dipolar interaction, we resort to the stochastic Liouville equation (SLE) of Kubo (1954) and Anderson (1954), rather than to second-order perturbation theory. In agreement with previous work (Papon et al., 1968; Leblond et al., 1971a), our analysis shows that the characteristic time scale against which the dipolar correlation time should be compared is the electronic T_2 relaxation time.

In the next two subsections we summarize the time-domain analysis of Paper I.

2.2 Rate equations

The dynamics of the electronic polarization, P_S, is justifiably taken to be independent of the dipolar interaction with the nuclear spins, as other mechanisms relax the electrons more efficiently. With R_{1S} denoting the rate of electronic T_1 relaxation, and v_1 the rate constant of the mw excitation of the (allowed) EPR transition, the rate equation of the electronic polarization is

$$\dot{P}_S = -R_{1S}(P_S - P_S^{\text{eq}}) - 2v_1 P_S. \tag{4}$$

Here P_S^{eq} is the equilibrium (Boltzmann) electronic polarization and the dot over the symbol denotes differentiation with respect to time. Solving this equation for P_S^{ss} at steady state, we arrive at the ratio

$$p = \frac{P_S^{\text{ss}}}{P_S^{\text{eq}}} = \frac{R_{1S}}{R_{1S} + 2v_1} = 1 - s, \tag{5}$$

where s is the familiar electronic saturation factor. We refer to p as the electronic polarization factor, since $p = 0$ indicates that the steady-state polarization has vanished and $p = 1$ indicates that it is identical to the Boltzmann polarization (i.e., maximally polarized).

The rate equation of the nuclear polarization, P_I, is

$$\dot{P}_I = -R_{1I}(P_I - P_I^{\mathrm{eq}}) - v_+ P_I - v_- P_S, \tag{6}$$

where R_{1I} is the nuclear T_1 relaxation rate, and the phenomenological rate constants $v_\pm$ quantify the mw excitation of the forbidden transitions. The steady state of (6) is

$$R_{1I}(P_I^{\mathrm{ss}} - P_I^{\mathrm{eq}}) = -v_+ P_I^{\mathrm{ss}} - p v_- P_S^{\mathrm{eq}}, \tag{7}$$

where $P_S^{\mathrm{ss}} = p P_S^{\mathrm{eq}}$ was used in the last term.

As the derivations in Sec. 3 consider only the effect of mw excitation, we have written (7) such that the relaxation contribution is on the left and the mw contribution on the right of the equality. Subsequently, to identify the phenomenological rate constants $v_\pm$, we will match the terms on the right-hand side with the predictions of the proper analysis in liquids.

From (7) we find the DNP enhancement

$$\epsilon = P_I^{\mathrm{ss}}/P_I^{\mathrm{eq}} - 1 = \epsilon_{\mathrm{SE}} - (1 - p_X), \tag{8}$$

where the first equality is the definition of ϵ and

$$\epsilon_{\mathrm{SE}} = \frac{p v_-}{R_{1I} + v_+} \frac{|\gamma_S|}{\gamma_I}, \qquad p_X = \frac{R_{1I}}{R_{1I} + v_+}. \tag{9}$$

From ϵ_{SE} it is clear that the solid effect benefits from large $p v_-$ and small $R_{1I} + v_+$. The ratio p_X in (9) is analogous to the electronic polarization factor (5), and we call it nuclear cross-polarization factor. In liquids, v_+ is typically negligible compared to the nuclear spin-lattice relaxation rate, and $p_X \approx 1$. Then,

$$\epsilon_{\mathrm{SE}} \approx (p v_-) T_{1I} |\gamma_S|/\gamma_I \qquad (p_X \approx 1). \tag{10}$$

2.3 Spin dynamics

The dynamics of the quantum-mechanical expectation values s_n of the electronic spin operators S_n ($n = x, y, z$) is described by the classical Bloch equations

$$\begin{bmatrix} \dot{s}_x \\ \dot{s}_y \\ \dot{s}_z \end{bmatrix} = - \begin{bmatrix} R_{2S} & \Omega & 0 \\ -\Omega & R_{2S} & \omega_1 \\ 0 & -\omega_1 & R_{1S} \end{bmatrix} \begin{bmatrix} s_x \\ s_y \\ s_z \end{bmatrix} + R_{1S} \begin{bmatrix} 0 \\ 0 \\ s_z^{\mathrm{eq}} \end{bmatrix}. \tag{11}$$

The matrix in (11) contains the electronic transverse relaxation rate R_{2S}, the mw nutation frequency ω_1, and the offset $\Omega = \omega_S - \omega$ between the electronic Larmor frequency ω_S and the mw frequency ω.

In Paper I we visualized such coupled differential equations diagrammatically. In our visual depiction, the time derivative of a dynamical variable, like s_n, is represented by an oval node. The contributions to this time derivative, which are on the right-hand side of the differential equation, are represented by arrows that flow into that node (fig. 2a). The contribution of a given
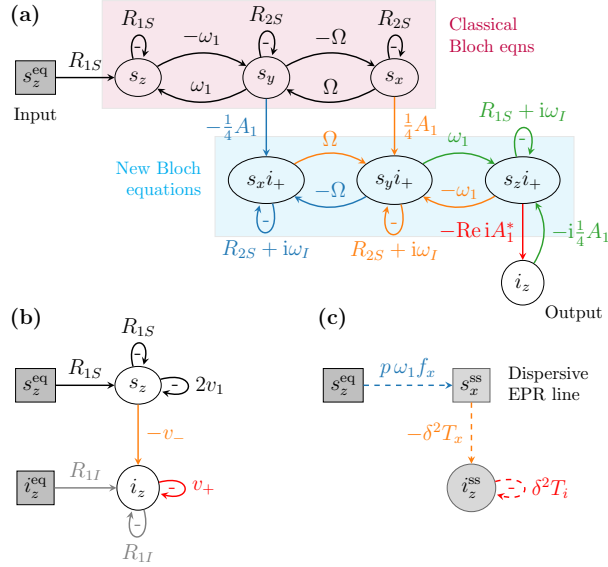
Figure 2. Diagrammatic representation of (**a**) the equations of motion of the spin dynamics relevant to the solid effect and (**b**) the rate equations of the polarizations. (**c**) Steady-state relationships between the variables.

arrow is obtained by multiplying the weight of the arrow with the variable from which the arrow originates. The self-arrows that exit from an oval node and enter the same node correspond to the relaxation terms along the diagonal of the Bloch matrix. The negative sign of the weight of a self-arrow is written separately inside the loop formed by the arrow. The constant variable s_z^{eq} in the inhomogeneous term of the Bloch equations (11) is represented by a gray rectangular node. With this notation, the Bloch equations (11) are depicted by the four nodes in the top row of fig. 2a and by the black arrows connecting these nodes.

The lower half of fig. 2a shows the dynamics of the electron-nuclear coherences that are relevant for the solid effect. In particular, the quantum-mechanical expectation values of the operators $S_n I_+$ ($n = x, y, z$), which we denote interchangeably by g_n and $s_n i_+$, evolve according to the following coupled differential equations (Sezer, 2023):

$$
\begin{bmatrix} \dot{g}_x \\ \dot{g}_y \\ \dot{g}_z \end{bmatrix} = -\mathscr{B} \begin{bmatrix} g_x \\ g_y \\ g_z \end{bmatrix} - i\frac{1}{4}A_1 \begin{bmatrix} -is_y \\ is_x \\ i_z \end{bmatrix}
\tag{12}
$$

where

$$
\mathscr{B} = \begin{bmatrix} R_{2S} + i\omega_I & \Omega & 0 \\ -\Omega & R_{2S} + i\omega_I & \omega_1 \\ 0 & -\omega_1 & R_{1S} + i\omega_I \end{bmatrix}.
\tag{13}
$$

The matrix $\mathscr{B}$ is essentially the Bloch matrix but with the nuclear Larmor frequency ω_I added as an imaginary part to its main diagonal. The time-derivatives of g_n in (12) are represented by the three oval nodes enclosed in the cyan rectangle in fig.

2a. The arrows between these nodes are seen to exactly replicate the classical Bloch equations in the rectangle above them. The inhomogeneous term in (12) couples the dynamics of the variables g_n to the transverse components of the electronic magnetization, on the one hand, and to the longitudinal component of the nuclear magnetization, on the other. All these couplings scale with the dipolar interaction A_1. They play an essential role in the solid effect, as they connect the Boltzmann electronic polarization to the nuclear polarization (labeled 'Input' and 'Output' in fig. 2a).

Lastly, the mw contribution to the dynamics of the operator I_z, whose expectation value is denoted by i_z, is

$$\dot{i}_z|_{\text{coh}} = -\text{Re}\{iA_1^* g_z\}, \tag{14}$$

where Re takes the real part of a complex number. In fig. 2a this equation is represented by the oval node i_z (labeled 'Output') and the red arrow flowing into it.

In liquids, the weights A_1 fluctuate randomly due to molecular diffusion. When extending the formalism to liquids (Sec. 3.3), we will transform the system of differential equations (12) to an SLE (Kubo, 1969) that describes the spin dynamics under random modulation of A_1.

For comparison, fig. 2b shows the dynamics of the longitudinal components implied by the rate-equations (4) and (6). Visual inspection of fig. 2a and fig. 2b makes clear that the rate constant v_- provides a reduced description of the complicated network connecting s_z to i_z. Similarly, the rate constant v_+ accounts for the self-influence of i_z mediated by the coherences in the second set of Bloch equations. In Paper I we identified the rates $v_\pm$ and v_1 by requiring that the dynamics in fig. 2a and fig. 2b reached identical steady states (Sezer, 2023).

At steady state, the three dynamical variables of the classical Bloch equations (11) were related to each other and to the electronic Boltzmann polarization as follows:

$$s_x^{\text{ss}} = (\omega_1 f_x)s_z^{\text{ss}}, \quad s_y^{\text{ss}} = -(\omega_1 f_y)s_z^{\text{ss}}, \quad s_z^{\text{ss}} = (R_{1S}f_z)s_z^{\text{eq}} \tag{15}$$

where

$$f_y = \frac{R_{2S}}{R_{2S}^2 + \Omega^2}, \quad f_x = \frac{\Omega}{R_{2S}}f_y, \quad f_z = \frac{1}{R_{1S} + \omega_1^2 f_y}. \tag{16}$$

(Comparing the last equality in (15) with (5) we found that $p = R_{1S}f_z$, and that the rate constant of the allowed EPR transition was $v_1 = \omega_1^2 f_y/2$.)

Solving the second set of Bloch equations (eq. (12)) at steady state, and substituting g_z^{ss} in (14), we obtain

$$\dot{i}_z|_{\text{coh}}^{\text{ss}} = -\delta^2 \text{Re}\left\{ \begin{bmatrix} 0 & 0 & 1 \end{bmatrix} \mathscr{B}^{-1} \begin{bmatrix} -is_y^{\text{ss}} \\ is_x^{\text{ss}} \\ i_z^{\text{ss}} \end{bmatrix} \right\} \tag{17}$$

where the dipolar interaction is isolated in

$$\delta^2 = (A_1^* A_1)/4. \tag{18}$$

Since the transverse components $s_{x,y}^{ss}$ are related to the Boltzmann polarization (eqs. (15)), the right-hand side of (17) is of the form

$$\dot{i}_z|_{\text{coh}}^{ss} = -\delta^2(T_i i_z^{ss} + T_s s_z^{eq}), \tag{19}$$

where

$$T_i = \begin{bmatrix} 0 & 0 & 1 \end{bmatrix} \text{Re}\{\mathcal{B}^{-1}\} \begin{bmatrix} 0 & 0 & 1 \end{bmatrix}^T = \text{Re}\{\mathcal{B}_{33}^{-1}\}$$

$$T_s = \begin{bmatrix} 0 & 0 & 1 \end{bmatrix} \text{Re}\{i\mathcal{B}^{-1}\} \begin{bmatrix} p\omega_1 f_y & p\omega_1 f_x & 0 \end{bmatrix}^T. \tag{20}$$

(The superscript T indicates transpose.) Because $\mathcal{B}$ has units of inverse time, T_i and T_s have units of time.

We note that T_s receives contributions from both s_y^{ss} and s_x^{ss}. As was shown in Paper I, it is possible to rewrite the contribution of the former as if it also came from s_x^{ss}. In other words, the entire contribution of s_z^{eq} to the derivative of i_z at steady state can be expressed as if it is mediated only through the dispersive component s_x^{ss}, as depicted in fig. 2c. (Dashed arrows represent mathematical relationships between the variables that hold at steady state. Differently from the solid arrows, which correspond to causal dependencies governing the dynamics at all times, the dashed arrows need not reflect direct causal dependence. A rectangular node indicates that the inflowing arrows contribute directly to the value of the variable, and not to its time derivative. The gray shade of the nodes signals that the variables remain constant in time, as they should at steady state.)

In addition to $\mathcal{B}_{33}^{-1}$, where $\mathcal{B}_{ij}^{-1}$ is the ijth element of the inverse matrix $\mathcal{B}^{-1}$, in (20) we also need $\mathcal{B}_{31}^{-1}$ and $\mathcal{B}_{32}^{-1}$. These are $\mathcal{B}_{31}^{-1} = (\omega_1 F_x)F_z$, $\mathcal{B}_{32}^{-1} = (\omega_1 F_y)F_z$, and $\mathcal{B}_{33}^{-1} = F_z$, where the functions

$$F_y = \frac{R_{2S} + i\omega_I}{(R_{2S} + i\omega_I)^2 + \Omega^2}, \quad F_x = \frac{\Omega}{R_{2S} + i\omega_I}F_y$$

$$F_z = \frac{1}{R_{1S} + i\omega_I + \omega_1^2 F_y} \tag{21}$$

play an analogous role in the steady-state analysis of the second set of Bloch equations as the functions f_y, f_x and f_z (eq. (16)) in the classical Bloch equations. In terms of these,

$$T_i = \text{Re}\{F_z\}, \qquad T_s = (p\omega_1 f_x)T_x, \tag{22}$$

where

$$T_x = \text{Re}\{iF_z(\omega_1 F_y')\}, \qquad F_y' = \frac{2R_{2S} + i\omega_I}{R_{2S} + i\omega_I}F_y. \tag{23}$$

(The functions in (23) emerge from lumping the contribution of s_y^{ss} to that of s_x^{ss}, as mentioned above.)

With T_i and T_s determined, the forbidden-transition rates on the right-hand side of (7) become

$$v_+ = \delta^2(T_i - T_i^0), \quad pv_- = \delta^2 T_s = (p\omega_1 f_x)\delta^2 T_x, \tag{24}$$

where the mw-independent part of T_i, namely

$$T_i^0 = \text{Re}\{F_z(\omega_1 = 0)\} = (R_{1S} + i\omega_I)^{-1}, \tag{25}$$

is subtracted in the first equality of (24) because it contributes to the the nuclear T_1 relaxation rate. (In fig. 2a this mw-independent part corresponds to the loop formed by the green arrow from i_z to g_z and the red arrow in the opposite direction.)

2.4 The solid effect

Using the rates (24) we rewrite the solid-effect DNP enhancement (eq. (9)) as

$$\epsilon_{\mathrm{SE}} = \frac{(p\omega_1 f_x)T_x}{R_{1I}/\delta^2 + (T_i - T_i^0)} \frac{|\gamma_S|}{\gamma_I}. \tag{26}$$

The functions $p\omega_1 f_x$, T_x and $(T_i - T_i^0)$ in this expression are visualized in, respectively, the first, second and third rows of fig. 3. The product of the first two rows, which appears in the numerator of (26), is shown in the fourth row of the figure. In the right margin of the figure, we have included the flow diagram from fig. 2c, which has been straightened here so that the weights of the arrows correspond to the respective rows. Note that the dipolar interaction strength, δ, and the nuclear spin-lattice relaxation rate were not needed to calculate the properties in the first four rows of the figure. (They will be needed for the last two rows.)

While different magnetic fields B_0 yield different relaxation times, for illustrative purposes we used the same electronic T_1 and T_2 times for X, Q, W and J bands. We additionally used the same mw field ($B_1 = 6\,\mathrm{G}$) at all bands. Hence, the steady state of the classical Bloch equations (fig. 3, first row) is identical across the four columns of the figure. The solid blue lines, which correspond to the dispersive component of the power-broadened EPR line, are identical but appear different due to the different resolution of the horizontal axes. The absorptive component is much smaller under the power-broadening conditions considered here and is not shown. However, its contribution is exactly accounted for in the analysis. (This was the reason for introducing the functions in (23).) Anticipating the liquid state, we observe that the classical Bloch equations are independent of the dipolar coupling A_1 (fig. 2a). Hence, the first row of fig. 3 will not change when going to liquids because we use identical relaxation rates.

The transfer functions T_x and $(T_i - T_i^0)$ encapsulate all relevant steady-state properties of the second set of Bloch equations, as well as their coupling to the classical Bloch equations and to i_z through the dipolar interaction (fig. 2a). These functions are visualized in the second and third rows of fig. 3 (orange and red lines). The colored solid lines are calculated using the equations given above and correspond to solids, subject to the (unrealistic) assumption of very fast spin diffusion. The black dashed lines are calculated as described in the next section and correspond to liquids. Clearly, the time-dependent modulation of the dipolar interaction in liquids has a dramatic effect on these functions.

The fourth row in fig. 3 shows the product of the blue lines in the first row and the orange lines in the second row, and corresponds to the total transfer function from the primary input, s_z^{eq}, to the ultimate output, i_z (fig. 2a). With the exception of X band, going from solids to liquids substantially reduces the peaks of pv_-. (We used identical relaxation parameters for liquids and solids to highlight the role of the dipolar correlation time.)

The transfer functions in the first four rows of fig. 3 depend only on the electronic relaxation times (assuming $T_{2I} \gg T_{1S}, T_{2S}$). To calculate the enhancement ϵ_{SE} and the nuclear cross-polarization factor, p_X, which are shown in the last two rows of fig. 3, we had to select specific values for R_{1I} and δ^2. For the latter, we used the ensemble-averaged static value from (3),

$$\langle \delta^2 \rangle = \frac{1}{4} \langle A_1^* A_1 \rangle = D_{\mathrm{dip}}^2 \frac{6\pi}{5} \frac{N}{3b^3}, \tag{27}$$
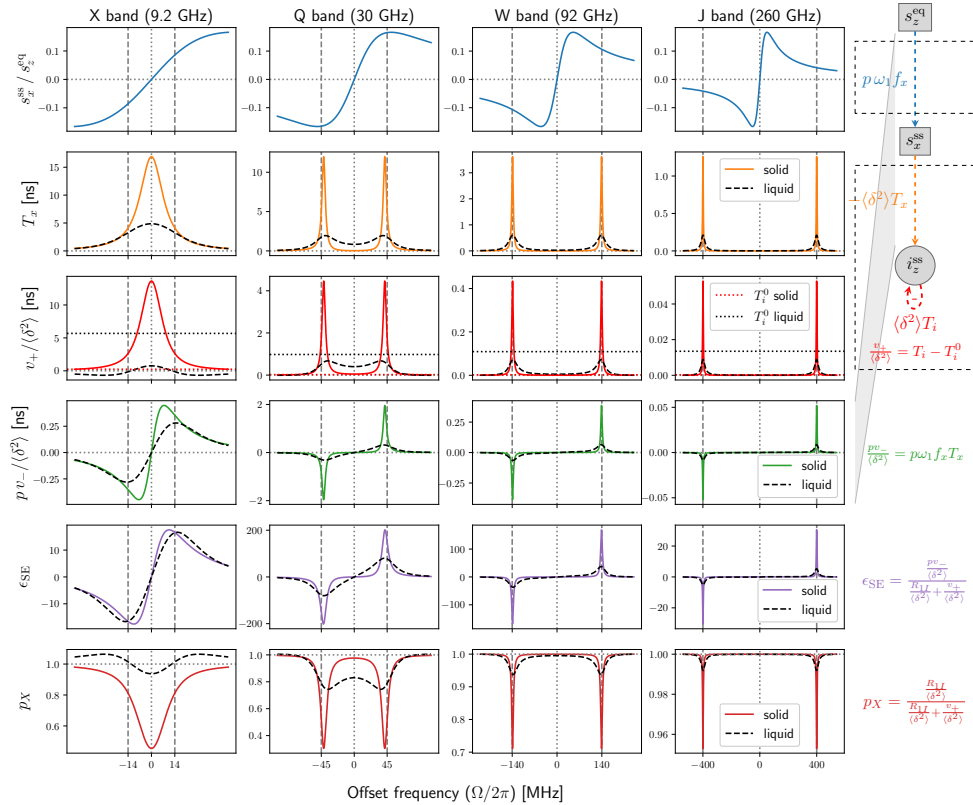
Figure 3. Comparison between solids (with fast spin diffusion) and liquids. 1st row: Dispersive component of the power-broadened EPR line. 2nd and 3rd rows: Relevant transfer functions of the new Bloch equations in fig. 2a. 4th row: The product of the first and second rows, which relates the input s_z^{eq} to the output i_z^{ss}. 5th row: DNP enhancement calculated from the third and fourth rows using $R_{1I}/\langle\delta^2\rangle$. 6th row: Nuclear cross-polarization factor calculated from the third row using $R_{1I}/\langle\delta^2\rangle$. Simulation parameters: $T_{2S} = 60$ ns, $T_{1S} = 9\,T_{2S}$, $B_1 = 6$ G (converted to ω_1 assuming $g = 2$), contact distance $b = 1$ nm, radical concentration $N = 0.1$ M, and T_{1I} of 4.7 ms (X band), 27.4 ms (Q band) and 50 ms (W and J bands). The dipolar correlation time of the liquid simulation (black dashed lines) is $\tau = T_{2S}/5 = 12$ ns.

which applies to solids with fast and efficient spin diffusion. The numerical calculations in fig. 3 are for contact distance $b_{ref} = 1$ nm and radical concentration $N_{ref} = 0.1$ M. These are realistic but otherwise arbitrary values.

270   For the purposes of illustration we wanted to use the same R_{1I} for all four mw bands in the figure. In this way, by comparing the four columns with each other, one would be able to assess the effect of changing only B_0. This strategy worked for solids, at least for the numerical values that were used, but failed for liquids due to the very different contributions of T_i to the nuclear relaxation rate (denoted by T_i^0 in (25)). This part of T_i is shown in the third row of fig. 3 with horizontal dotted lines. The red dotted lines for solids are very close to zero. The more visible black dotted lines for liquids change dramatically with the mw

275   band. Since the total relaxation rate R_{1I} must be larger than the contribution of T_i^0, the nuclear T_1 had to be only a few ms at X band. Using such small T_1 at J band, however, gave tiny liquid-state DNP enhancements.

Even if, admittedly, our calculated enhancements are only illustrative, in an effort to have somewhat realistic nuclear T_1 relaxation times, we used $T_{1I} = 50$ ms when the corresponding rate R_{1I} was larger than $\langle \delta^2 \rangle T_i^0$, and used $R_{1I}/\langle \delta^2 \rangle = 2T_i^0$ otherwise. This resulted in the following nuclear T_1 relaxation times: 4.7 ms (X band), 27.4 ms (Q band), and 50 ms (W and J bands). These were used for both liquids and solids. Naturally, the choice of different nuclear T_1 times has a direct influence on the calculated enhancements. For example, the peak DNP enhancements at X and W bands differ by about one order of magnitude (purple lines in the fifth row of fig. 3) mostly because the nuclear T_1 times at these two bands also differ by one order of magnitude.

The theory behind the liquid calculations in fig. 3 is presented in the next section.

3   Liquids

3.1   Molecular motion as a random process

Let us denote the components (r, θ, ϕ) of the inter-spin vector collectively by ζ. To describe the solid effect in liquids we consider a random process that changes ζ and thus modulates the dipolar interaction between the two types of spins.

When the random dynamics of ζ is modeled as a discrete-state process, the probabilities of observing the different discrete states are collected in the vector $\boldsymbol{p}(t)$. This probability vector evolves in time as $\dot{\boldsymbol{p}}(t) = -\mathbf{K}\boldsymbol{p}(t)$, where the matrix $\mathbf{K}$ contains the rate constants of the random transitions between the states. All eigenvalues of such stochastic matrices are non-negative and, for an ergodic chain of states, only one of the eigenvalues equals zero. In general, the stochastic matrix $\mathbf{K}$ is not symmetric, which means that there are a right eigenvector and a left eigenvector associated with each eigenvalue. The right eigenvector of the zero eigenvalue corresponds to the vector of equilibrium probabilities, $\boldsymbol{p}^{\mathrm{eq}}$, and the left eigenvector of the zero eigenvalue corresponds to the vector $\mathbf{1}$, which contains ones in all of its entries. Note that $\mathbf{1}^T \boldsymbol{p}^{\mathrm{eq}} = 1$.

When the random dynamics of ζ is modeled as a continuous-state diffusion process, then the time-evolution of the probability density $p(\zeta, t)$ is described by a Fokker-Planck equation of the form

$$\frac{\partial p(\zeta, t)}{\partial t} = -K_\zeta p(\zeta, t), \tag{28}$$

where K_ζ is a linear differential operator acting on the ζ dependence of $p(\zeta, t)$. As in the discrete case, the eigenvalues of K_ζ would be non-negative and one eigenvalue would equal zero. The corresponding right eigenfunction is the equilibrium probability density $p^{\mathrm{eq}}(\zeta)$, and the left eigenfunction is constant in ζ.

For brevity, we will adopt the discrete notation also for the continuous case. In particular, we will use italic bold symbols to indicate the dependence on ζ, and will denote operators that act on the ζ dependence with non-italicized capital bold symbols. With this understanding

$$\dot{\boldsymbol{p}}(t) = -\mathbf{K}\boldsymbol{p}(t) \tag{29}$$

will apply to both the continuous and discrete cases. Similarly, $\mathbf{1}^T \boldsymbol{f}$ will imply integration over the ζ dependence of the function $f(\zeta)$ in the continuous case, and summation over all different states in the discrete case.

Note that in the probabilistic description of the random process by the Fokker-Planck equation (28), the probability density $p(\zeta, t)$ characterizes an ensemble of nuclei, and ζ is treated as an independent variable which is not a function of t. In contrast, when a single nucleus is followed in time (e.g., through molecular dynamics simulations), ζ is a random function of t. Although this second picture of random trajectories was invoked when writing the dipolar correlation function (2), in the following pages we only work with the probabilistic description of an ensemble of identical nuclei.

Below, we will use the dynamical rule (29) when combining the stochastic dynamics of ζ with the spin dynamics from Sec. 2. The combined dynamics will be described by a stochastic Liouville equation (SLE) for a ζ-conditioned spin variable. In the case of the nuclear polarization, for example, the SLE will describe the dynamics of $\boldsymbol{P}_I(t)$, which stands for $P_I(\zeta, t)$ in the continuous case. For a detailed explanation of SLE the reader is referred to the literature (Kubo, 1969; Gamliel and Levanon, 1995). A more recent discussion can be found in Kuprov (2016).

3.2 Rate equations in liquids

3.2.1 Electronic polarization

The electronic polarization was assumed to be insensitive to the dipolar coupling with the nuclear spins. Hence, the ζ-conditioned electronic polarization $\boldsymbol{P}_S(t)$ is of the following separable form

$$\boldsymbol{P}_S(t) = \boldsymbol{p}^{\mathrm{eq}} P_S(t), \tag{30}$$

in which all ζ dependence is isolated in the equilibrium probability of the stochastic process. From $\boldsymbol{P}_S(t)$ we obtain the averaged (over ζ) electronic polarization by summing/integrating over the ζ dependence. This is done with the help of the constant vector/function $\mathbf{1}$ as follows:

$$\mathbf{1}^T \boldsymbol{P}_S(t) = \mathbf{1}^T \boldsymbol{p}^{\mathrm{eq}} P_S(t) = P_S(t). \tag{31}$$

(In the last equality we used the normalization of the probability, $\mathbf{1}^T \boldsymbol{p}^{\mathrm{eq}} = 1$, which reads $\int \mathrm{d}\zeta \, p^{\mathrm{eq}}(\zeta) = 1$ in the continuous case). Note that $P_S(t)$ in (30) is, in fact, the electronic polarization averaged over the stochastic variable (eq. (31)).

In this description, the experimentally accessible polarizations correspond to the averaged values, while the ζ-dependent variables, like $\boldsymbol{P}_S(t)$, serve only an intermediate, book-keeping role. In other words, at the end we will always average over ζ by using the constant vector/function $\mathbf{1}$.

Since (30) holds in general for the electronic polarization, it also holds at steady state and at equilibrium:

$$\boldsymbol{P}_S^{\mathrm{ss}} = \boldsymbol{p}^{\mathrm{eq}} P_S^{\mathrm{ss}}, \qquad \boldsymbol{P}_S^{\mathrm{eq}} = \boldsymbol{p}^{\mathrm{eq}} P_S^{\mathrm{eq}}. \tag{32}$$

Here P_S^{ss} and P_S^{eq} are the averaged (over ζ) values which correspond to the macroscopic polarization.

Lastly, we point out that at equilibrium all joint spin-ζ properties are of the above separable form. In other words, the last equality in (32) is not limited to the electronic polarization but applies to all other equilibrium properties.

3.2.2 Nuclear polarization

To illustrate the SLE formalism and to introduce further notation, we start by transforming the rate equation of the nuclear polarization (6) to an SLE:

$$\dot{\boldsymbol{P}}_I(t) = -\mathbf{K}\boldsymbol{P}_I(t) - \mathbb{R}_{1I}(\boldsymbol{P}_I(t) - \boldsymbol{p}^{\mathrm{eq}}P_I^{\mathrm{eq}})$$

340
$$- \mathbb{V}_+\boldsymbol{P}_I(t) - \mathbb{V}_-\boldsymbol{p}^{\mathrm{eq}}P_S(t). \tag{33}$$

There are several different things going on here, so let us examine them one by one.

First, following the convention introduced above, $\boldsymbol{P}_I(t)$ stands for $P_I(\zeta,t)$ which is the nuclear polarization conditional on the random state ζ. In this case the dot indicates partial derivative with respect to the time dependence, at fixed ζ. Second, the term $\mathbf{K}\boldsymbol{P}_I$ drives the dynamics in the ζ-space by providing "off-diagonal" elements that mix the different random states. All

345 remaining terms on the right-hand side of the SLE are "diagonal" in the ζ-space and act only on the spin degree(s) of freedom (which are conditioned on ζ). Third, the mw excitation rates $v_\pm$ and the relaxation rate R_{1I} have acquired ζ dependence, turning into operators in ζ space that act on $\boldsymbol{P}_I(t)$ or $\boldsymbol{p}^{\mathrm{eq}}$. In the discrete case, these would be matrices with different $v_\pm$ and R_{1I} values for each discrete state ζ along their main diagonals. We use hollow capital letters to denote such "diagonal" operators in ζ-space, also in the continuous case. Fourth, as all equilibrium properties, the nuclear Boltzmann polarization is

350 separable, with the ζ dependence confined to the equilibrium probability of the random process.

The steady state of the SLE (33) is

$$(\mathbf{K} + \mathbb{R}_{1I} + \mathbb{V}_+)\boldsymbol{P}_I^{\mathrm{ss}} = (P_I^{\mathrm{eq}}\mathbb{R}_{1I} - P_S^{\mathrm{eq}}p\mathbb{V}_-)\boldsymbol{p}^{\mathrm{eq}}, \tag{34}$$

where we used $P_S^{\mathrm{ss}} = pP_S^{\mathrm{eq}}$ (eq. (5)). Our aim is to solve (34) for $\boldsymbol{P}_I^{\mathrm{ss}}$ and then obtain the macroscopic nuclear polarization by calculating the average $P_I^{\mathrm{ss}} = \mathbf{1}^T\boldsymbol{P}_I^{\mathrm{ss}}$.

355 Clearly, solving (34) consists of calculating the inverse of the operator $(\mathbf{K} + \mathbb{R}_{1I} + \mathbb{V}_+)$. This is a daunting task in general, and requires the matrix representation of $\mathbf{K}$ in some basis set. Here we will limit the discussion to random motions that are orders of magnitude faster than the nuclear T_1 relaxation rate, which we concluded to be the case even in viscous liquids like glycerol. This assumption ensures that, at steady state, all nuclear spins in the sample are equivalent and have the same polarization. Hence, we will look for a separable steady-state solution of the form

360 $$\boldsymbol{P}_I^{\mathrm{ss}} = \boldsymbol{p}^{\mathrm{eq}}P_I^{\mathrm{ss}} \qquad \text{(ansatz for liquids).} \tag{35}$$

With this ansatz (34) becomes

$$(\mathbf{K} + \mathbb{R}_{1I} + \mathbb{V}_+)\boldsymbol{p}^{\mathrm{eq}}P_I^{\mathrm{ss}} = (P_I^{\mathrm{eq}}\mathbb{R}_{1I} - P_S^{\mathrm{eq}}p\mathbb{V}_-)\boldsymbol{p}^{\mathrm{eq}}. \tag{36}$$

While the difference between (34) and (36) appears to be minor, in fact we have achieved a tremendous simplification since $\mathbf{K}\boldsymbol{p}^{\mathrm{eq}} = 0$, and thus the dynamical aspect of the random process is gone; only its equilibrium (i.e., time-independent) properties

365 remain. Indeed, since in (36) all ζ-operators act on the equilibrium probability $\boldsymbol{p}^{\mathrm{eq}}$, integration over the ζ dependence brings

the average values:

$$\langle \mathbb{R}_{1I} \rangle = \mathbf{1}^T \mathbb{R}_{1I} \boldsymbol{p}^{\mathrm{eq}}, \qquad \langle \mathbb{V}_{\pm} \rangle = \mathbf{1}^T \mathbb{V}_{\pm} \boldsymbol{p}^{\mathrm{eq}}. \tag{37}$$

(These are the average values of the ζ-dependent functions $R_{1I}(\zeta)$ and $v_{\pm}(\zeta)$, respectively.) After averaging (36) becomes

$$(\langle \mathbb{R}_{1I} \rangle + \langle \mathbb{V}_{+} \rangle) P_I^{\mathrm{ss}} = \langle \mathbb{R}_{1I} \rangle P_I^{\mathrm{eq}} - p \langle \mathbb{V}_{-} \rangle P_S^{\mathrm{eq}}. \tag{38}$$

370   Comparison of (38) and (7) shows that the phenomenological rates R_{1I} and $v_{\pm}$ in the rate equation should be identified with the macroscopic averages $\langle R_{1I} \rangle$ and $\langle \mathbb{V}_{\pm} \rangle$ over the liquid sample. This is the familiar regime of fast motion, where one observes the averaged values of the magnetic parameters. We have thus provided a formal justification of why the averaged δ^2 in (27) corresponds to fast spin diffusion in the case of solids.

We observe that the static averages over 3D space, which are implied by (37), do not allow for the partial dynamical averaging
375 of the dipolar interaction. As discussed above, such averaging should be based on the time-correlation function of A_1. However the rate constants $v_{\pm}$ always contain the square of the dipolar interaction, and do not provide access to A_1 itself. We thus conclude that the partial averaging of the dipolar interaction in liquids is inaccessible to modeling by rate equations.

3.3   Spin dynamics in liquids

To gain access to the dipolar interaction before it is squared, we turn to the equations of motion of the coherences from Sec.
380 2.3. We first transform the equation of i_z (eq. (14)) to an SLE:

$$\dot{\boldsymbol{i}}_z(t)|_{\mathrm{coh}} = -\mathbf{K}\boldsymbol{i}_z(t) - \mathrm{Re}\{i\mathbb{A}_1^* \boldsymbol{g}_z(t)\}. \tag{39}$$

As before, $\boldsymbol{i}_z(t)$ and $\boldsymbol{g}_z(t)$ stand for $i_z(\zeta,t)$ and $g_z(\zeta,t)$ in the continuous case, $\mathbf{K}$ acts on the ζ dependence of $\boldsymbol{i}_z$, and A_1^* has become a "diagonal" operator in ζ-space. Averaging (39) over ζ we obtain the macroscopic equation

$$\mathbf{1}^T \dot{\boldsymbol{i}}_z(t)|_{\mathrm{coh}} = -\mathrm{Re}\{i\mathbf{1}^T \mathbb{A}_1^* \boldsymbol{g}_z(t)\}. \tag{40}$$

385 At steady state, using the ansatz (35) in the form $\boldsymbol{i}_z^{\mathrm{ss}} = \boldsymbol{p}^{\mathrm{eq}} i_z^{\mathrm{ss}}$, we have

$$\dot{i}_z|_{\mathrm{coh}}^{\mathrm{ss}} = -\mathrm{Re}\{i\mathbf{1}^T \mathbb{A}_1^* \boldsymbol{g}_z^{\mathrm{ss}}\}. \tag{41}$$

Since we accounted only for the coherent contribution to the time derivative of i_z, the right-hand side of (41) corresponds to the right-hand side of (7). Our aim is to identify the phenomenological rate constants $v_{\pm}$ that should be used in (7) by analyzing $\mathrm{Re}\{i\mathbf{1}^T \mathbb{A}_1^* \boldsymbol{g}_z^{\mathrm{ss}}\}$. However, because the random modulation of A_1 additionally contributes to the nuclear T_1 relaxation, we have
390 the equality

$$\mathrm{Re}\{i\mathbf{1}^T \mathbb{A}_1^* \boldsymbol{g}_z^{\mathrm{ss}}\} = R_{1I}^A i_z^{\mathrm{ss}} + v_+ i_z^{\mathrm{ss}} + p v_- s_z^{\mathrm{eq}} \tag{42}$$

from which we will read out the desired rates.

3.3.1 Contribution to T_1 relaxation

The contribution of $\mathrm{Re}\{\mathrm{i}\mathbf{1}^T\mathbb{A}_1^* \boldsymbol{g}_z^{ss}\}$ to the nuclear spin-lattice relaxation can be identified by its value in the absence of mw irradiation. From (12) and (13) we see that for $\omega_1 = 0$ the dynamics of g_z completely decouples from g_x and g_y. The SLE of $\boldsymbol{g}_z$ in this case becomes

$$\dot{\boldsymbol{g}}_z(t) = -\mathbf{K}\boldsymbol{g}_z(t) - (R_{1S} + \mathrm{i}\omega_I)\boldsymbol{g}_z(t) - \mathrm{i}\frac{1}{4}\mathbb{A}_1\boldsymbol{i}_z(t). \tag{43}$$

Technically, R_{1S} and ω_I should be operators that act on the ζ dependence of $\boldsymbol{g}_z$. However we take the electronic T_1 relaxation rate and the nuclear Larmor frequency to be independent of the dipolar coupling, which is parametrized by ζ. The corresponding operators are then $R_{1S}\mathbb{I}$ and $\omega_I\mathbb{I}$, where $\mathbb{I}$ is the identity operator in ζ-space. This identity operator will not be written explicitly.

The steady-state solution of (43) is

$$\boldsymbol{g}_z^{ss} = -\mathrm{i}\frac{1}{4}(\mathbf{K} + R_{1S} + \mathrm{i}\omega_I)^{-1}\mathbb{A}_1\boldsymbol{p}^{eq}i_z^{ss}, \tag{44}$$

where we again used the ansatz for liquids. Substituting this $\boldsymbol{g}_z^{ss}$ on the left-hand side of (42) we find that the nuclear relaxation rate due to A_1 is

$$R_{1I}^A = \frac{1}{4}\mathrm{Re}\{\mathbf{1}^T\mathbb{A}_1^*(\mathbf{K} + R_{1S} + \mathrm{i}\omega_I)^{-1}\mathbb{A}_1\boldsymbol{p}^{eq}\}. \tag{45}$$

To express this relaxation rate in a more intelligible manner, we observe that the inverse of a matrix M whose eigenvalues have strictly positive real parts can be written as

$$M^{-1} = \int_0^\infty e^{-Mt}\,\mathrm{d}t. \tag{46}$$

Applying this identity to the matrix $(\mathbf{K} + R_{1S} + \mathrm{i}\omega_I)$ in (45) we find

$$R_{1I}^A = \frac{1}{4}\mathrm{Re}\{\int_0^\infty \mathrm{d}t\, e^{-(R_{1S}+\mathrm{i}\omega_I)t}C_{11}(t)\}, \tag{47}$$

where

$$\begin{aligned}
C_{11}(t) &= \mathbf{1}^T\mathbb{A}_1^* e^{-\mathbf{K}t}\mathbb{A}_1\boldsymbol{p}^{eq} \\
&= \int \mathrm{d}\zeta\, A_1^*(\zeta)e^{-K_\zeta t}A_1(\zeta)p^{eq}(\zeta)
\end{aligned} \tag{48}$$

is the time-correlation function of the dipolar interaction (eq. (2)). Since the integral in (47) corresponds to the Laplace transform

$$J_{11}(s) = \int_0^\infty \mathrm{d}t\, e^{-st}C_{11}(t), \tag{49}$$

we have

$$R_{1I}^A = \frac{1}{4}\text{Re}\{J_{11}(R_{1S} + \mathrm{i}\omega_I)\}. \tag{50}$$

The real part of the Laplace transform is known as spectral density. Here the spectral density is evaluated at a the complex argument $R_{1S} + \mathrm{i}\omega_I$, which contains both the nuclear Larmor frequency and the electronic T_1 relaxation rate.

420   Let us examine (50) in the solid-state limit where A_1 does not change with time. Then $C_{11} = \langle A_1^* A_1 \rangle$ and

$$R_{1I,\text{solid}}^A = \langle \delta^2 \rangle \frac{T_{1S}}{1 + T_{1S}^2 \omega_I^2}. \tag{51}$$

In Abragam's nomenclature (Abragam, 1961) this is relaxation of the second kind, meaning that it is due to the relaxation of the electronic spins and not due to the modulation of the dipolar interaction by motion. This $R_{1I,\text{solid}}^A / \langle \delta^2 \rangle$ was shown with horizontal, red dotted lines in the third row of fig. 3.

425   In the case of liquids, we expect $C_{11}(t)$ to decay with time. Assuming a mono-exponential decay with correlation time τ,

$$R_{1I,\text{exp}}^A = \langle \delta^2 \rangle \text{Re}\{ \int_0^\infty \mathrm{d}t\, e^{-(R_{1S} + \mathrm{i}\omega_I + \tau^{-1})t} \}$$

$$= \langle \delta^2 \rangle \text{Re}\{ (R_{1S} + \tau^{-1} + \mathrm{i}\omega_I)^{-1} \}. \tag{52}$$

This $R_{1I,\text{exp}}^A / \langle \delta^2 \rangle$ was shown with horizontal, black dotted lines in the third row of fig. 3. To understand why it increases with decreasing ω_I, let us examine the case of motion that is faster than the electronic T_1 time, i.e., $\tau^{-1} \gg R_{1S}$. The result,

$$R_{1I,\text{exp}}^A \approx \langle \delta^2 \rangle \frac{\tau}{1 + \tau^2 \omega_I^2}, \tag{53}$$

430 is relaxation of the first kind with Lorentzian spectral density. Clearly, smaller ω_I implies larger dipolar contribution to the nuclear T_1 relaxation rate.

     Having identified the relaxation rate R_{1I}^A on the right-hand side of (42), we now proceed with the analysis of the rates $v_\pm$ characterizing the forbidden transitions.

3.3.2   Contribution to forbidden transitions

435 Combining the dynamics of the coherences (eq. (12)) with the stochastic dynamics (eq. (29)), we arrive at the following SLE:

$$\begin{bmatrix} \dot{\boldsymbol{g}}_x \\ \dot{\boldsymbol{g}}_y \\ \dot{\boldsymbol{g}}_z \end{bmatrix} = -(\mathbf{K} + \mathscr{B}) \begin{bmatrix} \boldsymbol{g}_x \\ \boldsymbol{g}_y \\ \boldsymbol{g}_z \end{bmatrix} - \mathrm{i}\frac{1}{4}\mathbb{A}_1 \begin{bmatrix} -\mathrm{i}s_y \boldsymbol{p}^{\text{eq}} \\ \mathrm{i}s_x \boldsymbol{p}^{\text{eq}} \\ \boldsymbol{i}_z \end{bmatrix}. \tag{54}$$

Note that the matrix $\mathscr{B}$ does not depend on time as the electronic relaxation properties were taken to be insensitive to the dipolar interaction between the electronic and nuclear spins. Recall that the operators written as upright bold letters (including the hollow ones) act on the ζ dependence of the variables, which is encoded by the italic bold symbols. The script uppercase

440 letters denote 3×3 matrices, which act on the column vectors that are shown explicitly.

Although not shown explicitly in (54), we imply the tensor products of the operators $\mathbf{K}$, $\mathscr{B}$ and $\mathbb{A}_1$ with the identity operators in the spaces on which $\mathbf{K}$, $\mathscr{B}$ and $\mathbb{A}_1$ do not act (i.e., $\mathbf{K}$ and $\mathbb{A}_1$ are in fact $\mathcal{I} \otimes \mathbf{K}$ and $\mathcal{I} \otimes \mathbb{A}_1$ where $\mathcal{I}$ is the 3×3 identity matrix, and $\mathscr{B}$ is $\mathcal{B} \otimes \mathbb{I}$ where $\mathbb{I}$ is the identity operator in the ζ-space).

Before solving (54) at steady state, let us introduce the eigenvalue problem of $\mathscr{B}$,

$$\mathscr{B}\mathscr{V} = \mathscr{V}\mathcal{D}, \tag{55}$$

where the diagonal matrix

$$\mathcal{D} = \mathrm{diag}(\lambda_1, \lambda_2, \lambda_3) \tag{56}$$

contains the eigenvalues of $\mathscr{B}$ along its main diagonal, and the columns of the 3×3 matrix $\mathscr{V}$ contain the corresponding right eigenvectors. Then, the steady state of (54) is

$$\mathscr{V}(\mathbf{K}+\mathcal{D})\mathscr{V}^{-1}\begin{bmatrix} \boldsymbol{g}_x^{\mathrm{ss}} \\ \boldsymbol{g}_y^{\mathrm{ss}} \\ \boldsymbol{g}_z^{\mathrm{ss}} \end{bmatrix} = -\mathrm{i}\frac{1}{4}\mathbb{A}_1\boldsymbol{p}^{\mathrm{eq}}\begin{bmatrix} -\mathrm{i}s_y^{\mathrm{ss}} \\ \mathrm{i}s_x^{\mathrm{ss}} \\ i_z^{\mathrm{ss}} \end{bmatrix}, \tag{57}$$

which, after inverting the matrices, yields

$$\begin{bmatrix} \boldsymbol{g}_x^{\mathrm{ss}} \\ \boldsymbol{g}_y^{\mathrm{ss}} \\ \boldsymbol{g}_z^{\mathrm{ss}} \end{bmatrix} = -\mathrm{i}\frac{1}{4}\mathscr{V}(\mathbf{K}+\mathcal{D})^{-1}\mathbb{A}_1\boldsymbol{p}^{\mathrm{eq}}\mathscr{V}^{-1}\begin{bmatrix} -\mathrm{i}s_y^{\mathrm{ss}} \\ \mathrm{i}s_x^{\mathrm{ss}} \\ i_z^{\mathrm{ss}} \end{bmatrix}. \tag{58}$$

Plugging this solution for $\boldsymbol{g}_z^{\mathrm{ss}}$ into the left-hand side of (42), and defining the matrix

$$\mathcal{L} = \mathbf{1}^T\mathbb{A}_1^*(\mathbf{K}+\mathcal{D})^{-1}\mathbb{A}_1\boldsymbol{p}^{\mathrm{eq}}, \tag{59}$$

we find

$$\mathrm{Re}\{\mathrm{i}\mathbf{1}^T\mathbb{A}_1^*\boldsymbol{g}_z^{\mathrm{ss}}\} = \frac{1}{4}\mathrm{Re}\{\begin{bmatrix} 0 & 0 & 1 \end{bmatrix}\mathscr{V}\mathcal{L}\mathscr{V}^{-1}\begin{bmatrix} -\mathrm{i}s_y^{\mathrm{ss}} \\ \mathrm{i}s_x^{\mathrm{ss}} \\ i_z^{\mathrm{ss}} \end{bmatrix}\}. \tag{60}$$

Comparison with the right-hand side of (42) yields

$$\begin{aligned} R_{1I}^A + v_+ &= \frac{1}{4}\begin{bmatrix} 0 & 0 & 1 \end{bmatrix}\mathrm{Re}\{\mathscr{V}\mathcal{L}\mathscr{V}^{-1}\}\begin{bmatrix} 0 & 0 & 1 \end{bmatrix}^T \\ v_- &= \frac{1}{4}\begin{bmatrix} 0 & 0 & 1 \end{bmatrix}\mathrm{Re}\{\mathrm{i}\mathscr{V}\mathcal{L}\mathscr{V}^{-1}\}\begin{bmatrix} \omega_1 f_y & \omega_1 f_x & 0 \end{bmatrix}^T, \end{aligned} \tag{61}$$

where we used the relationships between $s_{x,y}^{\mathrm{ss}}$ and s_z^{eq} (eq. (15)) to arrive at v_-.

We observe that $\mathcal{L}$ is a 3×3 diagonal matrix without any ζ dependence since the right-hand side of (59) is averaged over ζ. With $\mathcal{L} = \mathrm{diag}(L_1, L_2, L_3)$, we have

$$L_n = \mathbf{1}^T\mathbb{A}_1^*(\mathbf{K}+\lambda_n)^{-1}\mathbb{A}_1\boldsymbol{p}^{\mathrm{eq}} \qquad (n = 1, 2, 3). \tag{62}$$

Using (46) these diagonal elements can be written as

$$
\begin{aligned}
L_n &= \mathbf{1}^T \mathbb{A}_1^* \int_0^\infty e^{-(\mathbf{K}+\lambda_n)t}\, dt\, \mathbb{A}_1 \boldsymbol{p}^{\text{eq}} \\
&= \int_0^\infty e^{-\lambda_n t} \left(\mathbf{1}^T \mathbb{A}_1^* e^{-\mathbf{K}t} \mathbb{A}_1 \boldsymbol{p}^{\text{eq}} \right) dt \\
&= \int_0^\infty e^{-\lambda_n t} C_{11}(t)\, dt = J_{11}(\lambda_n),
\end{aligned}
\tag{63}
$$

where we used (48) in the third equality, and (49) in the last one. Hence, each L_n is the Laplace transform of the time-correlation function $C_{11}(t)$ evaluated at the eigenvalue λ_n of $\mathscr{B}$. The matrix $\mathcal{L}$ to be used in (61) is thus

$$
\mathcal{L} = \text{diag}(J_{11}(\lambda_1), J_{11}(\lambda_2), J_{11}(\lambda_3)).
\tag{64}
$$

In summary, for any given set of parameters, we form the 3×3 matrix $\mathscr{B}$ (eq. (13)) and numerically calculate its eigenvalues and eigenvectors. The former are used in (64) to calculate $\mathcal{L}$. Sandwiching $\mathcal{L}$ by the eigenvectors, as required in (61), we arrive at the desired rates $v_\pm$. This prescription applies to any motional model describing the stochastic dynamics of the inter-spin vector. Different models will differ only in their spectral densities J_{11}.

From a mathematical point of view, the simplest case is a model with exponential dipolar correlation function, $C_{11}^{\text{exp}}(t) = \langle \delta^2 \rangle e^{-t/\tau}$, where τ is the correlation time. Then

$$
J_{11}^{\text{exp}}(s) = \langle \delta^2 \rangle \frac{1}{s + \frac{1}{\tau}} = \langle \delta^2 \rangle \tau \frac{1}{s\tau + 1}
\tag{65}
$$

and (64) becomes

$$
\mathcal{L}_{\text{exp}} = \langle \delta^2 \rangle \, \text{diag}\left(\frac{1}{\lambda_1 + \frac{1}{\tau}}, \frac{1}{\lambda_2 + \frac{1}{\tau}}, \frac{1}{\lambda_3 + \frac{1}{\tau}} \right).
\tag{66}
$$

All black dashed lines labeled 'liquid' in fig. 3 were calculated using (66) with $\tau = 12\,\text{ns}$.

Comparing v_+ and pv_- (fig. 3, third and fourth rows) between the solid and liquid cases, we see that at Q, W and J bands the fluctuations of the dipolar interaction have substantially broadened the lines centered at the canonical solid-effect offsets $\Omega \approx \pm\omega_I$, and have reduced the peak enhancements in liquids compared to solids (fifth row). At X band, where the two lines had already merged in the solid case, the effect of fluctuations is qualitatively different, although line broadening is also visible. Most strikingly, the rate v_+ is seen to become negative at offsets larger than ω_I, which leads to nuclear polarization factor (eq. (9)) that exceeds one (fig. 3, bottom row).

4 Closer look at liquids

4.1 Translational diffusion of hard spheres

A mono-exponential dipolar correlation function is a poor model of translational diffusion in liquids. The so-called force-free hard sphere (FFHS) model, which assumes spherical molecules that contain the spins at their centers, is a more realistic yet analytically tractable model (Ayant et al., 1975; Hwang and Freed, 1975). It is universally employed in the analysis of diverse magnetic-resonance measurements, including nuclear relaxation by paramagnetic impurities (Okuno et al., 2022) and DNP via the Overhauser effect (Franck et al., 2013).

Because the spins are taken to be at the centers of the spherical molecules, the FFHS model has only two parameters: the coefficient of translational diffusion, D, and the distance of the spins upon contact of the spherical molecules, b. These two parameters form the characteristic motional time scale of the model (Ayant et al., 1975):

$$\tau = b^2/D. \tag{67}$$

The Laplace transform of the dipolar correlation function of this model is (Ayant et al., 1975, eqs. (51) and (55))

$$J_{11}^{\text{ffhs}}(s) = \langle \delta^2 \rangle \tau \, \frac{(s\tau)^{\frac{1}{2}} + 4}{(s\tau)^{\frac{3}{2}} + 4(s\tau) + 9(s\tau)^{\frac{1}{2}} + 9}. \tag{68}$$

Using J_{11}^{ffhs} in (64) we calculated numerically the same properties as in fig. 3 but for the FFHS model. The results are shown with colored solid lines in fig. 4. For comparison, the model with mono-exponential correlation function from fig. 3 is also reproduced in fig. 4 with black dashed lines.

The general observation from fig. 3 that the fluctuation of the dipolar interaction broadens the solid-effect lines at $\Omega \approx \pm\omega_I$ is even more relevant for the FFHS model. Indeed, for the same dipolar time scale τ, the FFHS lines are much broader and, correspondingly, much smaller in peak amplitude than the lines of the exponential model. Hence, the FFHS model predicts significantly smaller DNP enhancements (fig. 4, second last row) compared to the exponential model with the same time scale τ. At X band, the negative values of v_+ are still present but their magnitude is substantially reduced (third row). The corresponding offsets where the nuclear polarization factor, p_X, is larger than one are similar in the two models but again the deviation from one is much smaller in the FFHS model (last row).

Overall, p_X in liquids is very close to one (last row of fig. 4, FFHS model), which indicates that v_+ is very small compared to R_{1I}. In such cases, the solid-effect DNP enhancement (eq. (9)) is well approximated by (10). This explains why the enhancement in the fifth row of fig. 4 is essentially a rescaled version of the row directly above it.

The substantial reduction of the peak intensities at the solid-effect offsets $\Omega \approx \pm\omega_I$ is accompanied by a smaller but still appreciable *increase* of the intensities at small offsets ($\Omega \approx 0$). This trend is visible both in the transition from the solid case to a mono-exponential correlation function (fig. 3, second row) and in the further transition to the FFHS model (fig. 4). The significance of this observation will become clear in Sec. 4.4 where we compare our calculations with the experiments of Kuzhelev et al. (2022).
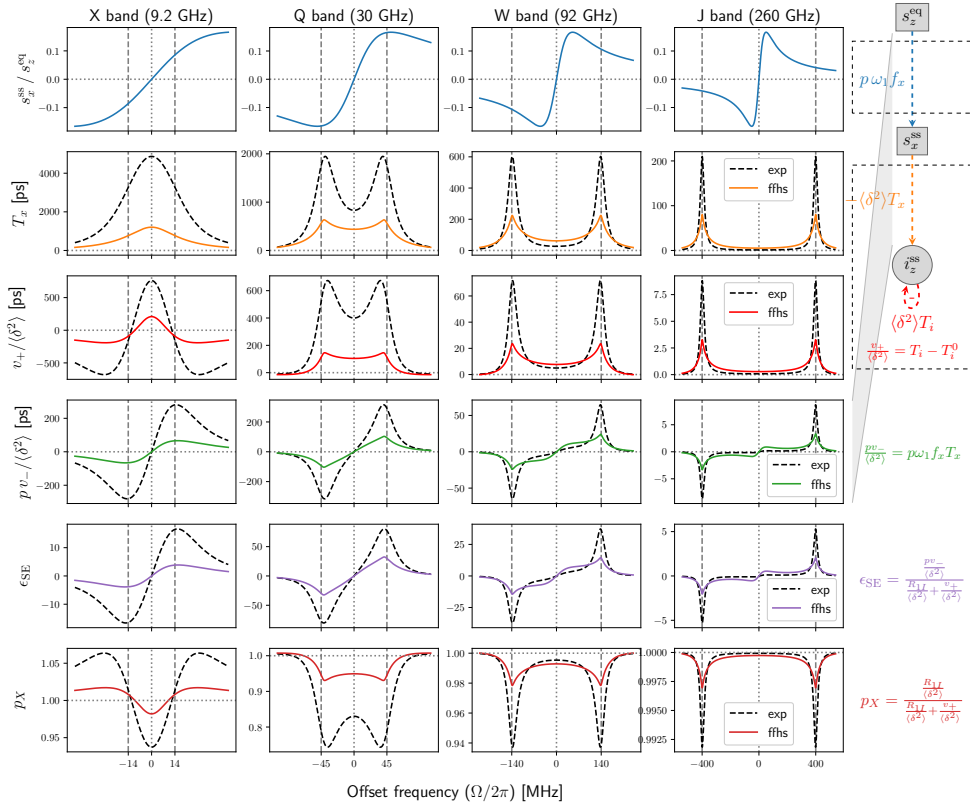
Figure 4. Same as fig. 3 for the model with exponential time-correlation function (black dashed lines) and the FFHS model (colored solid lines) both with $\tau = T_{2S}/5 = 12\,\mathrm{ns}$.

4.2 Approximate matrix inversion

Since $\mathscr{B}$ is a 3×3 matrix, its eigenvalues and eigenvectors are easily determined numerically, as we did when calculating the exponential and FFHS models in fig. 4. Nevertheless, to gain insight into the eigenvalue problem that is being solved, here we analyze (55) using perturbation theory. The analysis reveals that the eigenvalue problem is related to the effective magnetic field and the associated "tilted" coordinate frame (Wenckebach, 2016).

Let us introduce the matrix

$$
\mathscr{B}_0 = \begin{bmatrix} R_{2S} + \mathrm{i}\omega_I & \Omega & 0 \\ -\Omega & R_{2S} + \mathrm{i}\omega_I & \omega_1 \\ 0 & -\omega_1 & R_{2S} + \mathrm{i}\omega_I \end{bmatrix},
\tag{69}
$$

where R_{1S} in the lower right corner of $\mathscr{B}$ (eq. (13)) has been replaced by R_{2S}. The three eigenvalues of $\mathscr{B}_0$ are

$$
\lambda_{0,0} = R_{2S} + \mathrm{i}\omega_I, \quad \lambda_{0,\mp} = R_{2S} + \mathrm{i}(\omega_I \mp \omega_{\mathrm{eff}}),
\tag{70}
$$

where the frequency

$$\omega_{\mathrm{eff}} = \sqrt{\Omega^2 + \omega_1^2} \tag{71}$$

corresponds to the effective magnetic field in the rotating frame. This field is tilted away from the z axis by an angle α such that

$$\cos\alpha = \Omega/\omega_{\mathrm{eff}} = \mathrm{c}, \quad \sin\alpha = \omega_1/\omega_{\mathrm{eff}} = \mathrm{s}. \tag{72}$$

With the sine and cosine of α abbreviated as s and c, the eigenvectors of $\mathscr{B}_0$ are

$$\mathscr{V}_0 = \begin{bmatrix} \mathrm{s} & -\mathrm{c}/\sqrt{2} & -\mathrm{c}/\sqrt{2} \\ 0 & \mathrm{i}/\sqrt{2} & -\mathrm{i}/\sqrt{2} \\ \mathrm{c} & \mathrm{s}/\sqrt{2} & \mathrm{s}/\sqrt{2} \end{bmatrix} \tag{73}$$

where the first column corresponds to $\lambda_{0,0}$, the second to $\lambda_{0,-}$, and the third to $\lambda_{0,+}$. By inspection, $\mathscr{V}_0^{-1} = \mathscr{V}_0^H$, where the superscript H denotes Hermitian conjugation.

We treat the difference $\mathscr{B} - \mathscr{B}_0$ as a perturbation to $\mathscr{B}_0$. To first order in the perturbation the eigenvalues of the original matrix $\mathscr{B}$ are $\tilde{\lambda}_n = \lambda_{0,n} + v_{0,n}^H (\mathscr{B} - \mathscr{B}_0) v_{0,n}$ where $v_{0,n}$ is the nth column of $\mathscr{V}_0$. Using this expression we find the corrected eigenvalues

$$\tilde{\lambda}_0 = \tilde{R}_1 + \mathrm{i}\omega_I, \qquad \tilde{\lambda}_\mp = \tilde{R}_2 + \mathrm{i}(\omega_I \mp \omega_{\mathrm{eff}}), \tag{74}$$

with

$$\begin{aligned} \tilde{R}_1 &= R_{1S}(\cos\alpha)^2 + R_{2S}(\sin\alpha)^2 \\ \tilde{R}_2 &= R_{2S}[1 - (\sin\alpha)^2/2] + R_{1S}(\sin\alpha)^2/2. \end{aligned} \tag{75}$$

Collecting the eigenvalues (74) in the diagonal matrix $\tilde{\mathcal{D}} = \mathrm{diag}(\tilde{\lambda}_0, \tilde{\lambda}_-, \tilde{\lambda}_+)$, we have $\mathscr{B}^{-1} \approx \mathscr{V}_0 \tilde{\mathcal{D}}^{-1} \mathscr{V}_0^H$. As an example, the element in the lower right corner of the inverse matrix is

$$\mathscr{B}_{33}^{-1} = F_z \approx (\cos\alpha)^2 \tilde{\lambda}_0^{-1} + \frac{1}{2}(\sin\alpha)^2(\tilde{\lambda}_-^{-1} + \tilde{\lambda}_+^{-1}). \tag{76}$$

(This approximation of F_z was used in Paper I without proof.)

From (76), and using the first equality in (22), we immediately find

$$T_i \approx \mathrm{Re}\{\mathrm{c}^2 \tilde{\lambda}_0^{-1} + \mathrm{s}^2(\tilde{\lambda}_-^{-1} + \tilde{\lambda}_+^{-1})/2\}. \tag{77}$$

To obtain v_+, we need to subtract T_i^0 from T_i (eq. (24)). Since $\omega_1 = 0$ implies $s = 0$ and $c = 1$,

$$T_i^0 = \mathrm{Re}\{(R_{1S} + \mathrm{i}\omega_I)^{-1}\}, \tag{78}$$

which is identical to the exact result in (25). Hence,

$$v_+/\delta^2 \approx \mathrm{Re}\{\mathrm{s}^2(\tilde{\lambda}_-^{-1} + \tilde{\lambda}_+^{-1})/2 + \mathrm{c}^2\tilde{\lambda}_0^{-1} - (R_{1S} + \mathrm{i}\omega_I)^{-1}\}. \tag{79}$$

One can similarly obtain the rate constant v_- as a linear combination of the reciprocals of the approximate eigenvalues $\tilde{\lambda}_0$ and $\tilde{\lambda}_\mp$. The result is

$$T_x = \frac{\omega_1}{\omega_{\mathrm{eff}}^2}\mathrm{Re}\{\mathrm{i}X\} \tag{80}$$

with

$$X = R_{2S}\tilde{\lambda}_0^{-1} - \frac{1}{2}(R_{2S} + \mathrm{i}\omega_{\mathrm{eff}})\tilde{\lambda}_-^{-1} - \frac{1}{2}(R_{2S} - \mathrm{i}\omega_{\mathrm{eff}})\tilde{\lambda}_+^{-1}. \tag{81}$$

Recall that $v_-/\delta^2 = (\omega_1 f_x)T_x$ (eq. (24)).

The first eigenvalue in (74) does not depend on the offset Ω. The other two eigenvalues depend on the offset through ω_{eff}. Let us consider sufficiently large offsets such that $|\Omega| \gg \omega_1$, and so $\omega_{\mathrm{eff}} \approx |\Omega|$. This condition is satisfied at the solid-effect offset positions $\Omega \approx \pm\omega_I$ at W and J bands, but may be entirely inapplicable to X band at large mw powers, as discussed in Paper I. When the condition holds, $\mathrm{s} \approx 0$ and $\mathrm{c} \approx 1$, and the eigenvalues (74) become $\tilde{\lambda}_0 \approx R_{1S} + \mathrm{i}\omega_I$ and $\tilde{\lambda}_\mp \approx R_{2S} + \mathrm{i}(\omega_I \mp |\Omega|)$. Thus $\tilde{\lambda}_\mp^{-1}$ correspond to complex-valued Lorentzians centered at $\Omega = \pm\omega_I$ and with widths equal to the homogeneous EPR line width (without power-broadening). These are the Lorentzians that we see as narrow lines at W and J bands in the second and third rows of fig. 3 (orange and red solid lines).

In the case of motion, assuming mono-exponential correlation function for simplicity, each eigenvalue is replaced by $\tilde{\lambda}_n + 1/\tau$. This amounts to increasing the widths of the solid-effect Lorentzians from R_{2S} to $R_{2S} + 1/\tau$. The resulting motional broadening is the reason for the differences between the 'solid' and 'liquid' lines in the second and third rows of fig. 3.

For a general motional model, we have the approximate $\tilde{\mathcal{L}} = \mathrm{diag}(J_{11}(\tilde{\lambda}_0), J_{11}(\tilde{\lambda}_-), J_{11}(\tilde{\lambda}_+))$, which yields the approximation $\mathcal{V}\mathcal{L}\mathcal{V}^{-1} \approx \mathcal{V}_0\tilde{\mathcal{L}}\mathcal{V}_0^H$ to be used in (61). For the spectral density of the FFHS model, the perturbative expressions are compared with the exact numerical calculation in fig. 5. The former are plotted with black dashed-dotted lines and the latter with colored solid lines like in fig. 4. We see that the perturbative analysis is satisfactory in general, at least for the specific choice of parameters that were used. It gives excellent predictions for v_- (fig. 5, fourth row) and, because the two are related by a global scaling factor (eq. (10)), also for the DNP enhancement (fifth row). At the same time, it is seen to consistently fail for the rate v_+ at small offsets in the vicinity of the origin (third row).

We should mention that the perturbative approximation becomes progressively better when R_{2S} approaches R_{1S} (not shown), as it is exact for $R_{2S} = R_{1S}$.

Leaving the approximation quality of the perturbative analysis aside, we observe that the enhancement profiles in the fifth row of fig. 5 reveal the emergence of a novel feature at small offsets. At W band, this feature appears as a shoulder in the broadened lines, and at J band it is already separated from the canonical solid-effect peaks. Comparison with the lines in the first row of fig. 5 makes clear that this new feature in the DNP spectrum coincides with the extrema of the dispersive component of the power-broadened EPR line. For saturating mw powers, where $\omega_1 \gg R_{1S}R_{2S}$, these extrema occur at

$$\Omega_{1/2} = \omega_1\sqrt{T_{1S}/T_{2S}}. \tag{82}$$
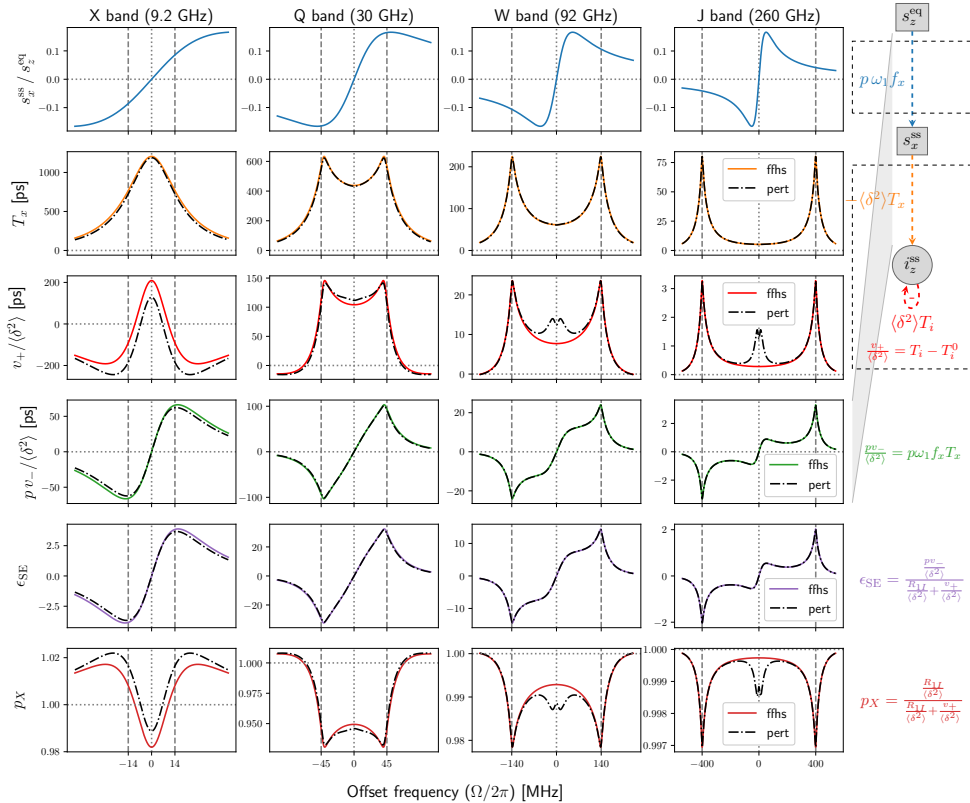
Figure 5. Comparison between the exact (solid colored lines) and perturbative (black dashed lines) calculations of the FFHS model. All parameters as in fig. 4. The eigenvalue problem of the generalized Bloch matrix $\mathscr{B}$ has a simple closed-form solution when $T_{1S} = T_{2S}$. The perturbative approximation uses these analytical eigenvectors and corrects the eigenvalues to first order in the difference $1/T_{1S} - 1/T_{2S}$.

(The subscript 1/2 was selected because these are also the offset positions where the electronic saturation factor equals one half.) The factor pv_- in the fourth row of fig. 5 is obtained as the product of the first and second rows, as elaborated in Paper I. When the solid-effect lines at $\Omega \approx \pm\omega_I$ (second row) become sufficiently broad, their amplitude at $\Omega_{1/2}$ gets large enough for the peak of the dispersive EPR line (first row) to be visible in the DNP spectrum.

4.3 Motional suppression and broadening

Let us examine more closely the suppression of the lines at the solid-effect offsets and the concurrent increase of their intensity at $\Omega_{1/2}$. We will limit the discussion to J band where the condition $\omega_I \gg \omega_1$ holds, and the solid-effect offsets are $\Omega = \pm\omega_I$. Using the perturbative eigenvalues (74), we see that only the real parts of $\tilde{\lambda}_{\mp}$ survive at these offsets. The peak amplitudes of the solid-effect lines are then proportional to $J_{11}(R_{2S})$.

The limits $\tau \ll T_{2S}$ and $\tau \gg T_{2S}$ correspond to, respectively, very fast and very slow diffusive motion relative to the electronic T_2. In the slow limit $\tau \gg T_{2S}$, we have

$$\lim_{R_{2S}\tau \to \infty} J_{11}(R_{2S})/\langle \delta^2 \rangle \to T_{2S} \tag{83}$$

for both the mono-exponential and FFHS motional models. This means that, in solids, the peaks increase with the electronic T_2. In the opposite limit of very fast motion, i.e., $\tau \ll T_{2S}$, we find

$$\lim_{R_{2S}\tau \to 0} \frac{J_{11}(R_{2S})}{\langle \delta^2 \rangle} \to \begin{cases} \tau & \text{exponential} \\ \dfrac{4}{9}\tau & \text{FFHS} \end{cases} \tag{84}$$

which means that, in liquids, the peak amplitudes are proportional to the dipolar correlation time τ. In other words, faster fluid diffusion (i.e., smaller τ) corresponds to smaller peaks, and thus smaller solid-effect enhancement at the canonical offsets. We also see that for the same τ the peaks of the FFHS model are less than half of the peaks of the exponential model, which is in agreement with fig. 4 (second and third rows).

To describe the transition between the fast and slow limits, we define the reduction factor

$$\rho(\tau) = \frac{1}{T_{2S}} \frac{J_{11}(R_{2S};\tau)}{\langle \delta^2 \rangle} \tag{85}$$

which equals one in the solid limit and approaches zero for small τ. Since it quantifies how much smaller the peaks are compared to the solid case, ρ is a measure of how "solid-like" the liquid is.

The top panel of fig. 6 shows the reduction factors of the exponential and FFHS models against the relative motional time scale τ/T_{2S}. For the exponential model, the solid-effect peaks drop to half of their maximum values at $\tau = T_{2S}$. In the case of the FFHS model, this happens already at $\tau \approx 4T_{2S}$ (see inset). In other words, appreciable reduction compared to the solid limit occurs even for exceedingly long diffusive time scales, several-fold the electronic T_2. For identical τ's the exponential model is seen to be more solid-like than the diffusive FFHS model across the entire motional range. Hence, realistic translational diffusion suppresses the solid-effect peaks more effectively than mono-exponential decay.

As a quantitative measure of the motional broadening, let us consider the magnitude of T_x (fig. 5, second row) at the locations of the extrema of the dispersive EPR line (first row). Since the intensity at these small offsets increases when going from the solid to the liquid case, we define the magnification factor

$$\mu(\tau) = \frac{T_x^{\text{liquid}}(\Omega_{1/2};\tau)}{T_x^{\text{solid}}(\Omega_{1/2})}. \tag{86}$$

This factor is shown in the bottom panel of fig. 6. For the FFHS model, the intensity at $\Omega_{1/2}$ is two to three orders of magnitude larger than the solid case across a broad range of motional time scales, between $\tau = T_{2S}$ and $\tau = 0.01T_{2S}$. Hence the peak of the dispersive EPR line should be magnified 100 to 1000 fold in liquids compared to the solid limit. It is also magnified for the mono-exponential dipolar correlation function, although not to the same extent.

In the light of these observations, next we analyze the DNP field profile of recent experiments with the free radical BDPA in DMPC lipid bilayers at 320 K (Kuzhelev et al., 2022).
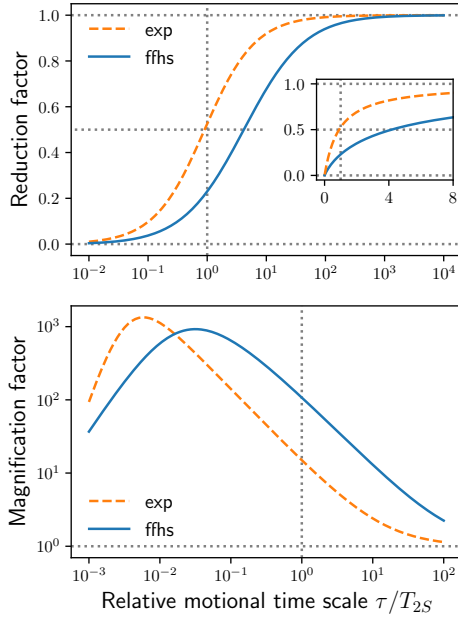
Figure 6. Multiplicative deviation of $T_x(\Omega)$ from the solid limit at (**a**) the solid-effect offsets $\Omega = \pm\omega_I$ and (**b**) the offsets $\Omega_{1/2} = \pm\omega_1\sqrt{T_{1S}/T_{2S}}$ for the exponential and FFHS models.

4.4 Comparison with experiment

620 The DNP experiments of Kuzhelev et al. (2022) were carried out at J band (260 GHz/400 MHz). For the acyl chain protons of the DMPC lipids, the peak DNP enhancements at the canonical solid-effect offsets were ± 12 (Kuzhelev et al., 2022). Two additional enhancement peaks of ± 8 were also observed at much smaller offsets. These were attributed to thermal mixing. Here we argue that they correspond to the extrema of the dispersive component of the EPR line.

The enhancements in Kuzhelev et al. (2022) were for BDPA-to-lipid ratio of 1:10 at a temperature of about 320 K. The room-
625 temperature EPR spectrum of BDPA at J band for this relatively high radical concentration was very narrow (Kuzhelev et al., 2022, fig. 2). The transverse relaxation time implied by this narrow line is $T_{2S} = 215$ ns. For the same radical concentration, the nuclear spin-lattice relaxation time at J band was 50 ms at 298 K (Kuzhelev et al., 2022). Although the experimental T_{1I} and T_{2S} are for 298 K, below we use these values to fit the DNP spectrum at 320 K. We also use $B_1 = 6$ G, as estimated in Kuzhelev et al. (2022).

630 In addition to these parameters with experimental support, three more parameters are needed for the calculation of the DNP enhancement: T_{1S}, τ, and $N/3b^3$. We will treat these as fitting parameters. Let us introduce the ratios

$$r_1 = \frac{T_{1S}}{T_{2S}}, \qquad r_2 = \frac{T_{2S}}{\tau}, \qquad r_3 = \frac{N/3b^3}{N_{\mathrm{ref}}/3b_{\mathrm{ref}}^3}. \tag{87}$$

The ratio r_1 expresses the unknown electronic T_1 relaxation time in terms of the known electronic T_2. From physical considerations, $r_1 \geq 1$. The ratio r_2 relates the diffusion time scale τ to the electronic T_2. Since T_{2S} is rather long, we expect τ to be shorter and hence $r_2 \geq 1$. Finally, the ratio r_3 expresses the actual factor $N/3b^3$, which is unknown, as a multiple of this same factor for arbitrarily selected reference values N_{ref} and b_{ref}. In principle, r_3 can be any positive number.

The mean volume per particle at a concentration of 1 M is $1.66\,\text{nm}^3$ and corresponds to a cube with side length of 1.18 nm. From molecular modeling, the "radius" of a BDPA molecule is about 0.6 nm, so it barely fits in the above cube. The partial molecular volume of a DMPC lipid in a lipid bilayer is $1.1\,\text{nm}^3$ (Greenwood et al., 2006). Thus, the concentration of one BDPA when surrounded by ten DMPC lipids cannot exceed $N_{\text{ref}} = 0.1\,\text{M}$, but is also likely close to this value. Additionally taking $b_{\text{ref}} = 1\,\text{nm}$ in the last equality of (87), we anticipate $r_3 > 1$.

From (10), the expected dependence of the DNP enhancement on the three fitting parameters can be written as

$$\epsilon_{\text{SE}} \approx p(r_1) v_-(r_1, r_2) r_3 \langle \delta_{\text{ref}}^2 \rangle T_{1I} |\gamma_S|/\gamma_I, \tag{88}$$

where $\langle \delta_{\text{ref}}^2 \rangle$ is calculated according to (27) using N_{ref} and b_{ref}. The ratio r_1, which determines $\Omega_{1/2}$ (eq. (82)), will influence the electronic polarization factor (or, equivalently, saturation factor). Together with the ratio r_2, it will also influence the forbidden transition rate v_-, although the effect of r_1 is expected to be small. From the previous discussion, we expect that r_2 will mostly be responsible for the width of the solid-effect lines that comprise v_-. Finally, r_3 will serve as a global scaling factor that will adjust the amplitude of the overall enhancement. Since the three fitting parameters are responsible for different features of the DNP spectrum, it should be possible to determine them uniquely.

The top plot in fig. 7 shows the experimental enhancements (red circles) together with the best fit obtained using the FFHS model with $B_1 = 6\,\text{G}$ (solid black line). The solid green line in this plot is the difference between the experimental data and the fit. The corresponding fitting parameters are shown in the first row of Table 1. Note that the fits were performed numerically using the exact expressions of p, $v_\pm$, and the DNP enhancement (eq. (9)), and were not restricted to the dependencies on the fitting parameters r_i ($i = 1, 2, 3$) that are indicated in (88). (For example, the general dependence of the electronic polarization factor p on T_{1S} and T_{2S} is not limited to the ratio T_{1S}/T_{2S}.)

After the fits converged, we used the final values of the fitting parameters to calculate the dispersive component of the EPR line $s_x^{\text{ss}} = p\omega_1 f_x s_z^{\text{eq}}$, and the factor T_x, such that $(p\omega_1 f_x)T_x = pv_-$. These are shown in the lower plot of fig. 7, where s_x^{ss} (blue) and T_x (orange) are scaled independently along the vertical axis. Their product (black dotted-dashed line) is also scaled independently along the y axis. Since $p_X \approx 1$ in our case, the product pv_- is itself proportional to the solid-effect enhancement. Hence the black lines in the upper and lower plots of fig. 7 are directly comparable. We can thus visually conclude that the unusual enhancement peaks at small offsets are a direct manifestation of the dispersive component of the power-broadened EPR line.

Because the mw field in the experiment is not known precisely, we also attempted fits with smaller B_1. The best fits were practically identical to the one shown in fig. 7 but with different values of the fitting parameters (Table 1). (The fit for $B_1 = 2\,\text{G}$ is shown in fig. A1 as an example.)
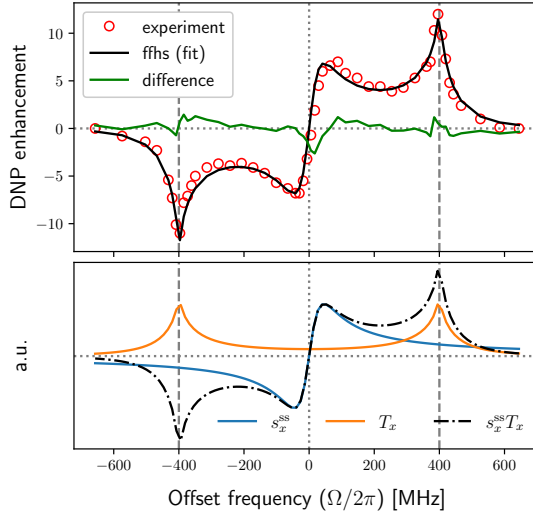
Figure 7. Experimental DNP field profile at J band (red circles) and fit with the FFHS model using $B_1 = 6\,\text{G}$ (solid black line). The central peaks in the enhancement profile follow the dispersive component of the power-broadened EPR line (solid blue line).

Table 1. Fitting parameters r_i ($i = 1, 2, 3$), and implied time scales (T_{1S} and τ) and contact distance (b). For different mw fields, r_1 changes such that $B_1\sqrt{r_1}$ remains constant.

B_1/G	r_1	r_2	r_3	T_{1S}/μs	τ/ns	b/nm[1]	$B_1\sqrt{r_1}$
6	7.2	30.4	8.9	1.5	7.07	0.482	16.088
5	10	30.4	13	2.2	7.08	0.427	16.065
4	16	30.3	20	3.5	7.09	0.368	16.047
3	29	30.3	36	6.1	7.10	0.304	16.034
2	64	30.3	80	14	7.10	0.232	16.025
1	257	30.3	321	55	7.11	0.146	16.022

[1]Assuming radical concentration $N = 0.1\,\text{M}$.

From Table 1 we see that all fits resulted in the same value of the parameter r_2, implying $\tau = 7.1\,\text{ns}$ for the motional time scale of the FFHS model. This parameter is very robust because it directly reflects the width of the experimental solid-effect lines at $\Omega = \pm\omega_I$. Although, normally, their line width should depend on both T_{2S} and τ, the exceptionally narrow EPR line puts us in the regime $\tau \ll T_{2S}$ where the influence of T_{2S} is negligible. As a result, the motional broadening of the solid-effect lines in the DNP spectrum reports directly on the diffusive time scale of BDPA in the lipid environment.

The fitting parameter r_1 adjusts the extrema of the dispersive EPR line (solid blue line in fig. 7), which are at $\Omega_{1/2} = \pm\omega_1\sqrt{r_1}$ (eq. (82)). By monitoring the product of $\sqrt{r_1}$ and B_1 in the last column of Table 1, we see that, each time B_1 is modified, the fitted r_1 changes such that $\Omega_{1/2}$ remains unchanged, as required by the positions of the non-canonical enhancement peaks in
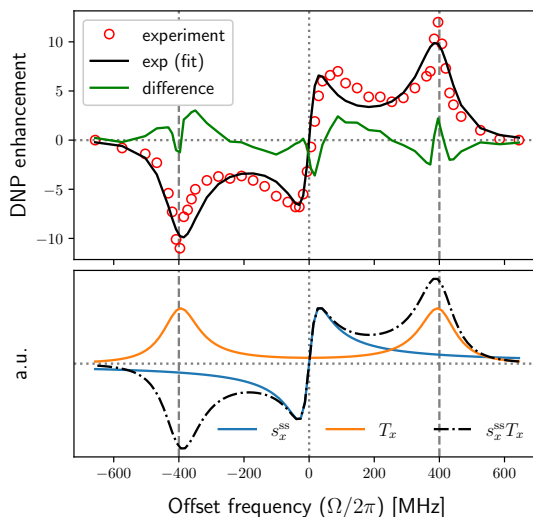
Figure 8. Same as fig. 7 for the model with mono-exponential dipolar correlation function and $B_1 = 6\,\mathrm{G}$ (solid black line). The fit parameters $r_1 = 3.6$, $r_2 = 89$, $r_3 = 7.7$ correspond to $T_{1S} = 0.77\,\mu\mathrm{s}$, $\tau = 2.4\,\mathrm{ns}$, $b = 0.507\,\mathrm{nm}$ (assuming $N = 0.1\,\mathrm{M}$).

the experimental data. However, because r_1 has to increase quadratically to compensate for the reduction of B_1, the implied
675   electronic T_1 times become exceedingly long (tens of microseconds) at the smaller values of B_1 (1-2 G).

When B_1 is reduced, the fitting parameter r_3 also increases quadratically to compensate for the dependence of the overall enhancement on ω_1^2. Assuming $N_{\mathrm{ref}} = 0.1\,\mathrm{M}$ is a good estimate of the actual concentration of BDPA in the lipid bilayer, it is possible to calculate a contact distance, b, from the fitted value of r_3. The deduced contact distances are given in the second last column of Table 1. Only the values for large B_1 (5-6 G) are in qualitative agreement with the molecular structure of BDPA.
680   In fig. 8 we show a fit to the same experimental data using a mono-exponential dipolar correlation function. While the difference between the data and the fit (green line in top panel of fig. 8) is not much worse than what we had for the FFHS model, it is apparent that the exponential model strives to find the right balance between the broadening of the solid-effect lines and the tails of these lines at the lower offsets, ultimately producing too broad solid-effect lines and too narrow non-canonical peaks. (An exponential fit with $B_1 = 4\,\mathrm{G}$ is shown in fig. A2.) We thus see that the J-band DNP spectrum clearly differentiates
685   between two alternative motional models, ruling out the less realistic one.

The most certain outcome of the fits with the FFHS model is the deduced motional time scale τ, as it comes directly from the width of the solid-effect lines (T_{2S} is too long to contribute). The deduced value of T_{1S} is somewhat less certain since it is accessed relative to T_{2S} and also depends on the mw field B_1. Nevertheless, with reasonable choices of T_{2S} and B_1, the fit to the non-canonical extrema in the DNP spectrum restricts T_{1S} to a meaningful window between $1.5\,\mu\mathrm{s}$ and $2.5\,\mu\mathrm{s}$
690   (Table 1). Least certain is the estimate of the contact distance b since, in addition to B_1, it requires precise knowledge of the radical concentration and the nuclear spin-lattice relaxation time. Although the latter is accessible experimentally, its value was measured at 298 K, while the DNP measurements are at 320 K.

In spite of the uncertainty in the estimated value of the distance parameter b, let us use τ and b in (67) to calculate the coefficient of relative translational diffusion. With $b = 0.482\,\text{nm}$ (Table 1, first row) and $\tau = 7.1\,\text{ns}$, we get $D = b^2/\tau = 0.033\,\text{nm}^2/\text{ns} = 33 \times 10^{-12}\,\text{m}^2/\text{s}$. Alternatively, with $b = 0.427\,\text{nm}$ (Table 1, second row) and $\tau = 7.1\,\text{ns}$, we find $D = 26 \times 10^{-12}\,\text{m}^2/\text{s}$. The first value corresponds to $B_1 = 6\,\text{G}$ and the second to $B_1 = 5\,\text{G}$.

For comparison, the coefficient of lateral diffusion of phospholipids in oriented DMPC bilayers, as determined from pulsed field gradient NMR, is about $11 \times 10^{-12}\,\text{m}^2/\text{s}$ at 308 K, $20 \times 10^{-12}\,\text{m}^2/\text{s}$ at 323 K, and $27 \times 10^{-12}\,\text{m}^2/\text{s}$ at 333 K (Filippov et al., 2003, fig. 5B, 0 mol% cholesterol). As the temperature of the DNP measurements is closer to the middle value, our two estimates of D are seen to be larger by a factor of 1.65 and 1.3, respectively.

However, the D of the FFHS model corresponds to the relative translational diffusion of the electronic and nuclear spins, i.e., $D = D_S + D_I$, where D_S and D_I denote the coefficients of translational diffusion of the two spin types. Disregarding all complicating factors, one could thus take $D_I = 20 \times 10^{-12}\,\text{m}^2/\text{s}$ from the literature value, and rationalize the values that we deduced from the width of the solid-effect DNP lines as implying either $D_S = 13 \times 10^{-12}\,\text{m}^2/\text{s}$ or $D_S = 6 \times 10^{-12}\,\text{m}^2/\text{s}$ for the diffusion coefficients of the free radical BDPA in the lipid bilayer. As the obtained numerical values are rather plausible, we conclude that the quantitative analysis of the J-band DNP spectrum leads to meaningful molecular properties. Without the theoretical framework developed in this paper, neither the molecular distance b nor the diffusion coefficient D would be accessible from a solid-effect DNP spectrum in the liquid state.

5 Concluding discussion

Erb, Motchane and Uebersfeld had the hunch that the dispersive component of the EPR line is reflected in the solid-effect DNP enhancement (Erb et al., 1958a). A theoretical justification of their intuition was provided in Paper I (Sezer, 2023). Here, the formalism was extended to the solid effect in liquids. Our theoretical predictions were compared with recent DNP measurements at high field (Kuzhelev et al., 2022). The comparison demonstrated that, under appropriate conditions, the dispersive component of the EPR line is literally visible in the field profile of the DNP enhancement. Provided that seeing is believing, we have thus closed the circle.

The DNP mechanism which became known as the solid-state effect due to Abragam (Abragam and Proctor, 1958) had been observed in liquids from the very beginning (Erb et al., 1958a, b). Nevertheless, perhaps because it yielded comparatively smaller absolute enhancements and often coexisted with the Overhauser effect (Leblond et al., 1971b), the solid effect has remained less explored in liquids compared to solids. The recent use of this DNP mechanism as a new modality for probing the molecular dynamics in ionic liquids (Neudert et al., 2017; Gizatullin et al., 2021b) and its first applications at high magnetic field (Kuzhelev et al., 2022), indicate that the potential of the solid effect in the liquid state is yet to be harvested. A theoretical understanding of the mechanism in liquids is clearly going to be helpful in these endeavors. Developing the needed theory has been the main aim of the companion and current papers.

Admittedly, a theoretical description of the solid effect in liquids was developed more than 50 years ago by Korringa and colleagues (Papon et al., 1968; Leblond et al., 1971a). In fact, their analysis was much more ambitious than ours, as it aimed

to quantify the DNP spectrum during the transition from the Overhauser effect to the solid effect upon reduction of the experimental temperature (Leblond et al., 1971b). Thus, in addition to the secular terms of the dipolar interaction that we considered here and in Paper I, their Hamiltonian also contained the non-secular terms, which are important for the cross-relaxation rates of the Overhauser effect, as well as the orientation dependent part of the electronic Zeeman interaction, which determines the electronic relaxation rates and thus the degree of saturation. Following the prescription of second-order time-dependent perturbation theory, Korringa et al. derived equations for the deviations of both the electronic and nuclear polarizations from their values at thermal equilibrium (Papon et al., 1968).

The analytical framework of Korringa and colleagues had two additional aspects. First, as is well known, the semi-classical description of spin-lattice relaxation relaxes the system to infinite temperature. The usual way of correcting for this shortcoming in magnetic resonance is to subtract the correct thermal equilibrium from the right-hand side of the dynamical equation of the density matrix (Abragam, 1961). Instead, Korringa (1964) imposed the correct temperature by writing the equation of motion of the density matrix for complex-valued time, whose imaginary part was proportional to the inverse temperature. This mathematical trick exploits the fact that a quantum-mechanical propagator with imaginary time becomes a Boltzmann factor. The analytical continuation to complex time modified the familiar Liouville-von Neumann equation of the density matrix to a form that is not common in magnetic resonance. Second, as an integral part of their formalism, Korringa et al. (1964) modeled the stochastic modulation of the spin Hamiltonian as rotational diffusion of one coordinate frame with respect to another, which led to an exponential correlation function with single decay time τ. It is not straightforward to see how their final analytical expressions should be modified if one were to use the FFHS model, for example.

In this context, it is worth mentioning that the mono-exponential model did not accurately fit the experimental data of Leblond et al. (1971b) and the authors took a Gaussian distribution for $\ln \tau$ (Leblond et al., 1971a). In fig. 8 we also observed that an exponential motional model did not fit the experimental DNP spectrum at J band (Kuzhelev et al., 2022), whereas the FFHS model with a single motional parameter did (fig. 7). One should remember, however, that the analysis of Leblond et al. (1971b) was performed four years before the spectral density of the FFHS model was solved analytically (Ayant et al., 1975; Hwang and Freed, 1975).

In spite of the differences between the analytical framework of Korringa and colleagues (Papon et al., 1968; Leblond et al., 1971a) and our approach, which hamper a direct comparison of the results, we observe that the derivations in their first paper (Papon et al., 1968) assumed isotropic electronic relaxation, i.e., $T_{1S} = T_{2S}$. As we saw in Sec. 4.2, in this case the matrix $\mathscr{B}$ (eq. (13)) becomes equal to $\mathscr{B}_0$ (eq. (69)) and the eigenvalue problem of the latter has a simple closed-form solution. All quantities of interest then become linear combinations of the reciprocals of the eigenvalues. Indeed, the final expressions of Papon et al. (1968) are linear combinations of Lorentzian spectral densities, which contain the effective frequency ω_{eff} (eq. (71)).

The assumption of equal longitudinal and transverse electronic relaxation rates was relaxed in the second paper (Leblond et al., 1971a). Sadly, this second paper has been cited only five times, and although all of the citing papers report new experiments, they do not use the theoretical expressions of Leblond et al. (1971a) to analyze the experimental data. One can only hope that, by being less ambitious, the theory developed in the current paper fares differently.

Appendix A: Additional figures
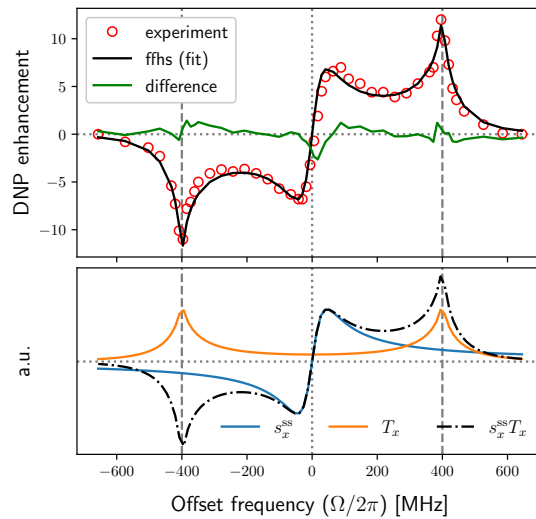
Figure A1. Same as fig. 7 (FFHS model) for $B_1 = 2\,\text{G}$ (solid black line). The fit parameters are given in the second last row of Table 1.
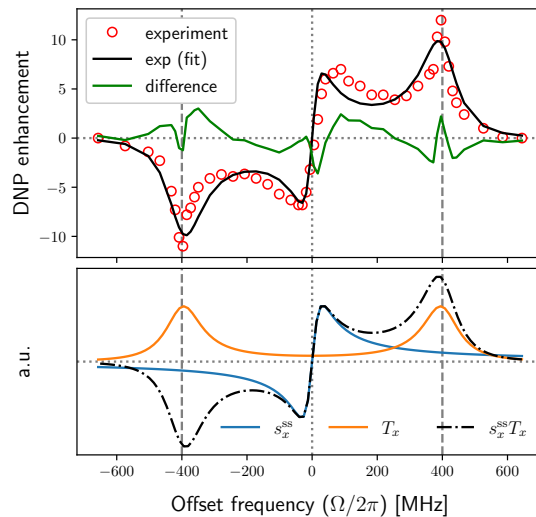
Figure A2. Same as fig. 8 (exponential model) for $B_1 = 4\,\text{G}$ (solid black line). The fit parameters $r_1 = 8.1$, $r_2 = 90$, $r_3 = 17$ correspond to $T_{1S} = 1.7\,\mu\text{s}$, $\tau = 2.4\,\text{ns}$, $b = 0.387\,\text{nm}$ (assuming $N = 0.1\,\text{M}$).

Author contributions. DS developed the theory and wrote the paper.

Competing interests. No competing interests are present.

Acknowledgements. Andrei Kuzhelev kindly provided the analyzed experimental data in electronic form. The initial stage of the reported
research was funded by grants to Thomas Prisner. Subsequent funding was provided by DFG grant 405972957. Stimulating discussions with
all members of the Prisner group are gratefully acknowledged.

765

References

Abragam, A.: The Principles of Nuclear Magnetism, Oxford University Press, New York, 1961.

Abragam, A. and Proctor, W. G.: Une nouvelle méthode de polarisation dynamique des noyaux atomiques dans les solides, Compt. rend., 246, 2253–2256, 1958.

Anderson, P. W.: A Mathematical Model for the Narrowing of Spectral Lines by Exchange or Motion, Journal of the Physical Society of Japan, 9, 316–339, https://doi.org/10.1143/JPSJ.9.316, 1954.

Ayant, Y., Belorizky, E., Alizon, J., and Gallice, J.: Calcul des densit'es spectrales r'esultant d'un mouvement al'eatoire de translation en relaxation par interaction dipolaire magn'etique dans les liquides, J. Phys. (Paris), 36, 991–1004, 1975.

Delage-Laurin, L., Palani, R. S., Golota, N., Mardini, M., Ouyang, Y., Tan, K. O., Swager, T. M., and Griffin, R. G.: Overhauser Dynamic Nuclear Polarization with Selectively Deuterated BDPA Radicals, Journal of the American Chemical Society, 143, 20 281–20 290, https://doi.org/10.1021/jacs.1c09406, 2021.

Denysenkov, V., Dai, D., and Prisner, T. F.: A triple resonance (e, 1H, 13C) probehead for liquid-state DNP experiments at 9.4 Tesla, Journal of Magnetic Resonance, 337, 107 185, https://doi.org/https://doi.org/10.1016/j.jmr.2022.107185, 2022.

Eills, J., Budker, D., Cavagnero, S., Chekmenev, E. Y., Elliott, S. J., Jannin, S., Lesage, A., Matysik, J., Meersmann, T., Prisner, T., Reimer, J. A., Yang, H., and Koptyug, I. V.: Spin Hyperpolarization in Modern Magnetic Resonance, Chemical Reviews, 123, 1417–1551, https://doi.org/10.1021/acs.chemrev.2c00534, 2023.

Erb, E., Motchane, J.-L., and Uebersfeld, J.: Effet de polarisation nucléaire dans les liquides et les gaz adsorbés sur les charbons, Compt. rend., 246, 2121–2123, 1958a.

Erb, E., Motchane, J.-L., and Uebersfeld, J.: Sur une nouvelle méthode de polarisation nucléaire dans les fluides adsorbés sur les charbons. extension aux solides et en particulier aux substances organiques irradiées., Compt. rend., 246, 3050–3052, 1958b.

Filippov, A., Orädd, G., and Lindblom, G.: The Effect of Cholesterol on the Lateral Diffusion of Phospholipids in Oriented Bilayers, Biophysical Journal, 84, 3079–3086, https://doi.org/https://doi.org/10.1016/S0006-3495(03)70033-2, 2003.

Franck, J. M., Pavlova, A., Scott, J. A., and Han, S.: Quantitative cw Overhauser effect dynamic nuclear polarization for the analysis of local water dynamics, Progress in Nuclear Magnetic Resonance Spectroscopy, 74, 33–56, https://doi.org/https://doi.org/10.1016/j.pnmrs.2013.06.001, 2013.

Gamliel, D. and Levanon, H.: Stochastic Processes in Magnetic Resonance, World Scientific, Singapore, 1995.

Gizatullin, B., Mattea, C., and Stapf, S.: Hyperpolarization by DNP and Molecular Dynamics: Eliminating the Radical Contribution in NMR Relaxation Studies, The Journal of Physical Chemistry B, 123, 9963–9970, https://doi.org/10.1021/acs.jpcb.9b03246, 2019.

Gizatullin, B., Mattea, C., and Stapf, S.: Field-cycling NMR and DNP –A friendship with benefits, Journal of Magnetic Resonance, 322, 106 851, https://doi.org/https://doi.org/10.1016/j.jmr.2020.106851, 2021a.

Gizatullin, B., Mattea, C., and Stapf, S.: Molecular Dynamics in Ionic Liquid/Radical Systems, The Journal of Physical Chemistry B, 125, 4850–4862, https://doi.org/10.1021/acs.jpcb.1c02118, 2021b.

Gizatullin, B., Mattea, C., and Stapf, S.: Three mechanisms of room temperature dynamic nuclear polarization occur simultaneously in an ionic liquid, Physical Chemistry Chemical Physics, 24, 27 004–27 008, https://doi.org/10.1039/D2CP03437A, 2022.

Greenwood, A. I., Tristram-Nagle, S., and Nagle, J. F.: Partial molecular volumes of lipids and cholesterol, Chemistry and Physics of Lipids, 143, 1–10, https://doi.org/https://doi.org/10.1016/j.chemphyslip.2006.04.002, 2006.

Holz, M., Heil, S. R., and Sacco, A.: Temperature-dependent self-diffusion coefficients of water and six selected molecular liquids for calibration in accurate 1H NMR PFG measurements, Phys. Chem. Chem. Phys., 2, 4740–4742, 2000.

805 Hovav, Y., Feintuch, A., and Vega, S.: Theoretical aspects of dynamic nuclear polarization in the solid state –The solid effect, Journal of Magnetic Resonance, 207, 176–189, https://doi.org/https://doi.org/10.1016/j.jmr.2010.10.016, 2010.

Hwang, L.-P. and Freed, J. H.: Dynamic effects of pair correlation functions on spin relaxation by translational diffusion in liquids, J. Chem. Phys., 63, 4017–4025, 1975.

Jakdetchai, O., Denysenkov, V., Becker-Baldus, J., Dutagaci, B., Prisner, T. F., and Glaubitz, C.: Dynamic Nuclear Polarization-
810 Enhanced NMR on Aligned Lipid Bilayers at Ambient Temperature, Journal of the American Chemical Society, 136, 15 533–15 536, https://doi.org/10.1021/ja509799s, 2014.

Korringa, J.: Dynamical Decomposition of a Large System, Physical Review, 133, A1228–A1229, https://doi.org/10.1103/PhysRev.133.A1228, 1964.

Korringa, J., Motchane, J. L., Papon, P., and Yoshimori, A.: Derivation of the Modified Bloch Equations for Spin Systems, Physical Review,
815 133, A1230–A1234, https://doi.org/10.1103/PhysRev.133.A1230, 1964.

Kubo, R.: Note on the Stochastic Theory of Resonance Absorption, Journal of the Physical Society of Japan, 9, 935–944, https://doi.org/10.1143/JPSJ.9.935, 1954.

Kubo, R.: A Stochastic Theory of Line Shape, pp. 101–127, https://doi.org/https://doi.org/10.1002/9780470143605.ch6, 1969.

Kuprov, I.: Fokker-Planck formalism in magnetic resonance simulations, Journal of Magnetic Resonance, 270, 124–135,
820 https://doi.org/https://doi.org/10.1016/j.jmr.2016.07.005, 2016.

Kuzhelev, A. A., Dai, D., Denysenkov, V., and Prisner, T. F.: Solid-like Dynamic Nuclear Polarization Observed in the Fluid Phase of Lipid Bilayers at 9.4 T, Journal of the American Chemical Society, 144, 1164–1168, https://doi.org/10.1021/jacs.1c12837, 2022.

Leblond, J., Papon, P., and Korringa, J.: Stochastic Theory of Dynamic Spin Polarization in Viscous Liquids with Anisotropic Electron-Spin Relaxation, Physical Review A, 4, 1539–1549, https://doi.org/10.1103/PhysRevA.4.1539, 1971a.

825 Leblond, J., Uebersfeld, J., and Korringa, J.: Study of the Liquid-State Dynamics by Means of Magnetic Resonance and Dynamic Polariza-tion, Physical Review A, 4, 1532–1539, https://doi.org/10.1103/PhysRevA.4.1532, 1971b.

Neudert, O., Mattea, C., and Stapf, S.: A compact X-Band resonator for DNP-enhanced Fast-Field-Cycling NMR, Journal of Magnetic Resonance, 271, 7–14, https://doi.org/https://doi.org/10.1016/j.jmr.2016.08.002, 2016.

Neudert, O., Mattea, C., and Stapf, S.: Molecular dynamics-based selectivity for Fast-Field-Cycling relaxome-
830 try by Overhauser and solid effect dynamic nuclear polarization, Journal of Magnetic Resonance, 276, 113–121, https://doi.org/https://doi.org/10.1016/j.jmr.2017.01.013, 2017.

Ni, Q. Z., Daviso, E., Can, T. V., Markhasin, E., Jawla, S. K., Swager, T. M., Temkin, R. J., Herzfeld, J., and Griffin, R. G.: High Frequency Dynamic Nuclear Polarization, Accounts of Chemical Research, 46, 1933–1941, https://doi.org/10.1021/ar300348n, 2013.

Okuno, Y., Schwieters, C. D., Yang, Z., and Clore, G. M.: Theory and Applications of Nitroxide-based Paramagnetic Cosolutes for Prob-
835 ing Intermolecular and Electrostatic Interactions on Protein Surfaces, Journal of the American Chemical Society, 144, 21 371–21 388, https://doi.org/10.1021/jacs.2c10035, 2022.

Papon, P., Motchane, J. L., and Korringa, J.: Unitary Theory of Dynamic Polarization of Nuclear Spins in Liquids and Solids, Physical Review, 175, 641–649, https://doi.org/10.1103/PhysRev.175.641, 1968.

Pinon, A. C., Capozzi, A., and Ardenkjær-Larsen, J. H.: Hyperpolarization via dissolution dynamic nuclear polarization: new technological and methodological advances, Magnetic Resonance Materials in Physics, Biology and Medicine, 34, 5–23, https://doi.org/10.1007/s10334-020-00894-w, 2021.

Prisner, T., Denysenkov, V., and Sezer, D.: Liquid state DNP at high magnetic fields: Instrumentation, experimental results and atomistic modelling by molecular dynamics simulations, Journal of Magnetic Resonance, 264, 68–77, https://doi.org/https://doi.org/10.1016/j.jmr.2015.11.004, 2016.

Sezer, D.: Dynamic view of the solid-state DNP effect, Magnetic Resonance (under review), https://doi.org/https://doi.org/10.5194/mr-2023-1, 2023.

Smith, A. A., Corzilius, B., Barnes, A. B., Maly, T., and Griffin, R. G.: Solid effect dynamic nuclear polarization and polarization pathways, The Journal of Chemical Physics, 136, 015 101, https://doi.org/10.1063/1.3670019, 2012.

Tan, K. O., Mardini, M., Yang, C., Ardenkjær-Larsen, J. H., and Griffin, R. G.: Three-spin solid effect and the spin diffusion barrier in amorphous solids, Science Advances, 5, eaax2743, https://doi.org/10.1126/sciadv.aax2743, 2019.

Tomlinson, D. J.: Temperature dependent self-diffusion coefficient measurements of glycerol by the pulsed N.M.R. technique, Molecular Physics, 25, 735–738, https://doi.org/10.1080/00268977300100661, 1973.

Wenckebach, T.: Essentials of Dynamic Nuclear Polarization, Spindrift Publications, The Netherlands, 2016.

Wenckebach, W. T.: Electron Spin–Spin Interactions in DNP: Thermal Mixing vs. the Cross Effect, Applied Magnetic Resonance, 52, 731–748, https://doi.org/10.1007/s00723-021-01335-0, 2021.

Wiśniewski, D., Karabanov, A., Lesanovsky, I., and Köckenberger, W.: Solid effect DNP polarization dynamics in a system of many spins, Journal of Magnetic Resonance, 264, 30–38, https://doi.org/https://doi.org/10.1016/j.jmr.2016.01.016, 2016.